Engineered fast-dissociating antibody fragments for multiplexed super-resolution microscopy

AUTHOR(S):

Zhang, Qianli; Miyamoto, Akitoshi; Watanabe, Shin; Arimori, Takao; Sakai, Masanori; Tomisaki, Madoka; Kiuchi, Tai; Takagi, Junichi; Watanabe, Naoki

CITATION:

Zhang, Qianli ...[et al]. Engineered fast-dissociating antibody fragments for multiplexed super-resolution microscopy. Cell Reports Methods 2022, 2(10): 100301.

ISSUE DATE:

2022-10-24

URL:

http://hdl.handle.net/2433/276855

Cell Reports
Methods

Article

Engineered fast-dissociating antibody fragments for multiplexed super-resolution microscopy

Graphical abstract

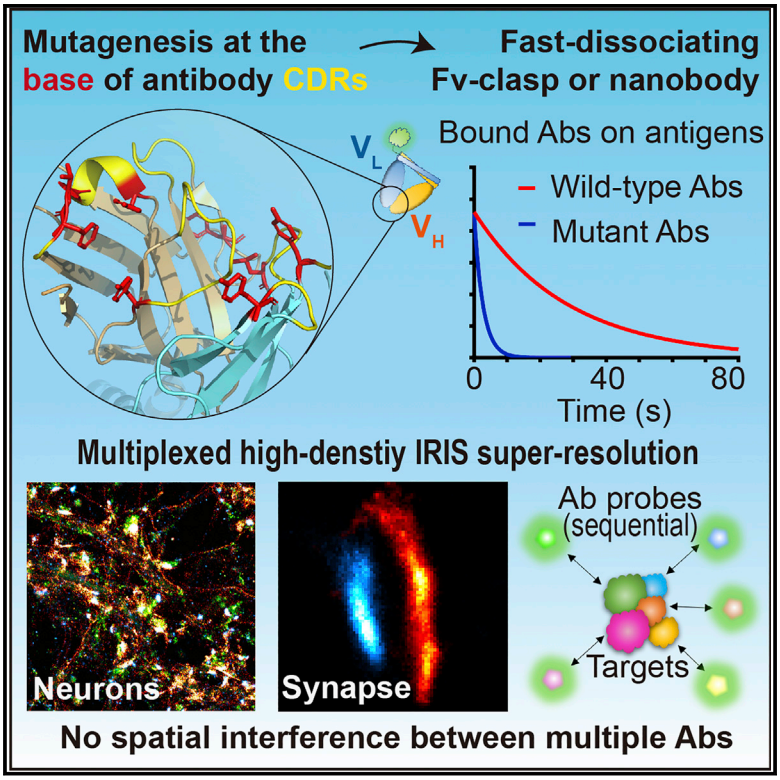

Highlights

- Mutagenesis at the base of CDRs accelerates dissociation of antibody fragments
- The mutagenesis strategy can be applied to off-the-shelf antibodies and nanobodies
- Fast-dissociating probes enable multiplexed and high-density IRIS super-resolution
- Probe accessibility is affected by Ab interference in other SMLM but not in IRIS

Authors

Qianli Zhang, Akitoshi Miyamoto, Shin Watanabe, ..., Tai Kiuchi, Junichi Takagi, Naoki Watanabe

Correspondence

watanabe.naoki.4v@kyoto-u.ac.jp

In brief

Zhang et al. establish a versatile mutagenesis strategy to efficiently increase the dissociation rate of antibodies without compromising binding specificity. Engineered fast-dissociating antibody fragments enable high-density IRIS multiplexed super-resolution imaging, which overcomes the intrinsic sparse labeling problem caused by spatial interference between multiple antibodies in other super-resolution approaches.

Zhang et al., 2022, Cell Reports Methods 2, 100301
October 24, 2022
https://doi.org/10.1016/j.crmeth.2022.100301

CellPress

Cell Reports Methods

CellPress OPEN ACCESS

Article

Engineered fast-dissociating antibody fragments for multiplexed super-resolution microscopy

Qianli Zhang,[1] Akitoshi Miyamoto,[1] Shin Watanabe,[1] Takao Arimori,[2] Masanori Sakai,[3] Madoka Tomisaki,[1] Tai Kiuchi,[4] Junichi Takagi,[2] and Naoki Watanabe[1,4,5,*]

[1]Laboratory of Single-Molecule Cell Biology, Kyoto University Graduate School of Biostudies, Kyoto 606-8501, Japan
[2]Institute for Protein Research, Osaka University, Suita, Osaka 565-0871, Japan
[3]Kyoto University Faculty of Engineering, Kyoto 606-8317, Japan
[4]Department of Pharmacology, Kyoto University Graduate School of Medicine, Kyoto 606-8501, Japan
[5]Lead contact
*Correspondence: watanabe.naoki.4v@kyoto-u.ac.jp
https://doi.org/10.1016/j.crmeth.2022.100301

MOTIVATION IRIS super-resolution microscopy achieves high-fidelity multiplexed imaging using exchangeable probes that transiently bind to targets. Nevertheless, generation of a fast-dissociating binder for each target has been challenging. The repository of antibody is expanding rapidly. Therefore, we developed a generalizable engineering strategy to generate fast-dissociating recombinant antibodies for IRIS imaging from off-the-shelf antibodies. The strategy could effectively increase the dissociation rate of existing antibodies by orders of magnitude. In addition, we examined the superiority of IRIS over conventional super-resolution microscopies in eliminating interference between multiple antibody-based probes in multiplexed high-density imaging.

SUMMARY

Image reconstruction by integrating exchangeable single-molecule localization (IRIS) achieves multiplexed super-resolution imaging by high-density labeling with fast exchangeable fluorescent probes. However, previous methods to develop probes for individual targets required a great amount of time and effort. Here, we introduce a method for generating recombinant IRIS probes with a new mutagenesis strategy that can be widely applied to existing antibody sequences. Several conserved tyrosine residues at the base of complementarity-determining regions were identified as candidate sites for site-directed mutagenesis. With a high probability, mutations at candidate sites accelerated the off rate of recombinant antibody-based probes without compromising specific binding. We were able to develop IRIS probes from five monoclonal antibodies and three single-domain antibodies. We demonstrate multiplexed localization of endogenous proteins in primary neurons that visualizes small synaptic connections with high binding density. It is now practically feasible to generate fast-dissociating fluorescent probes for multitarget super-resolution imaging.

INTRODUCTION

Single-molecule localization-based super-resolution microscopy surpasses the diffraction limit (~200 nm) of conventional optical microscopy. However, the imaging fidelity is limited by the labeling density and spatial interference between bulky antibodies in a confined resolved area (Kiuchi et al., 2015). A novel multitarget super-resolution approach named image reconstruction by integrating exchangeable single-molecule localization (IRIS) has overcome this problem by utilizing exchangeable fast-dissociating probes (IRIS probes) (Kiuchi et al., 2015). The initial IRIS probes were derived from peptides that bind to the endogenous target proteins. Transient binding probes have been recently developed based on peptide-peptide and peptide-protein interactions (Eklund et al., 2020; Farrell et al., 2022; Oi et al., 2020; Tas et al., 2021). However, these probes visualize only exogenous peptide-tagged targets, and only a few probes are available. Previously, we reported the development of IRIS probes by screening fast-dissociating monoclonal antibodies (Miyoshi et al., 2021). Although several antibody-based IRIS probes have been developed, the validation and production processes are still challenging. Generating recombinant probes from existing antibody sequences could greatly expand the usability of IRIS, but such an approach would require an efficient strategy to optimize the dissociation of the antibody-target interaction without compromising the binding specificity.

Antibody variable fragments (Fv) and nanobodies are small proteins that only contain the antigen-binding domains of

antibodies. The specific binding properties of these nanoscopic molecules make them suited for a variety of biological assays and medical applications (Dong et al., 2019). These small antibody fragments improve the localization accuracy by reducing the distance between the fluorescent signal and the target protein (Harris et al., 1998; Pleiner et al., 2015; Vallet-Courbin et al., 2017). The binding specificity of antibody fragments is governed by six complementarity-determining regions (CDRs) that form loops on the variable heavy chain (V_H) and light chain (V_L). A major challenge in antibody optimization is the trade-off between antibody affinity, specificity, stability, and solubility (Rabia et al., 2018). Enhanced affinity, for instance, sometimes leads to decreases in antibody specificity and stability (Houlihan et al., 2015; Tiller et al., 2017).

Individual Fv are unstable owing to the insufficient interaction between V_H and V_L. As a work around, a single-chain variable fragment (scFv) is a commonly used recombinant Fv, in which the V_H and V_L of the antibody are connected with a short linker peptide of 10–25 amino acids (Arimori et al., 2017). However, scFv cannot be adapted to all antibodies without stability engineering (Lehmann et al., 2015). Moreover, scFvs have a reduced stability under thermal stress, which may limit their potential as an imaging tool (Kang and Seong, 2020). To enhance the structural stability of the Fv, a universally applicable antibody fragment format, Fv-clasp, was constructed by fusing a coiled-coil SARAH domain of human Mst1 kinase to each chain of the variable region (Arimori et al., 2017). Fv-clasp constructs exhibit excellent compatibility and stability while retaining the binding affinity of the original antibodies (Arimori et al., 2017) and can be used for immunostaining (Watson et al., 2021).

Here, we introduce an efficient strategy to generate IRIS probes by site-specific mutagenesis of the common residues within V_H and V_L domains in the either a Fv-clasp or nanobody format. Eight IRIS probes coupled with a set of peptide tags (FLAG tag, hemagglutinin [HA] tag, TARGET tag, V5 tag, S tag, and ALFA tag) and two neuronal proteins (Homer and VGlut) were generated by modifying antibody cDNAs from hybridoma clones and open-source antibody sequences. These mutated antibody fragments retained their specificity and were usable for IRIS super-resolution microscopy by conjugating fluorescent proteins to their C terminus. Our method enables rapid conversion of existing antibody cDNAs to fast-dissociating probes for multiplexed analyses and will greatly expand the library of IRIS super-resolution imaging probes.

RESULTS

Construction of recombinant Fv based on Fv-clasp

We obtained a set of epitope tag-specific antibody sequences from previous studies, including P20.1 (anti-TARGET tag) (Tabata et al., 2010), 12CA5 (anti-HA tag) (Arimori et al., 2017), 2H8 (anti-FLAG tag) (Ikeda et al., 2017), V302A (anti-V5 tag) (Miyoshi et al., 2021), S66B (anti-S tag) (Miyoshi et al., 2021), and 11G9 (anti-FLAG tag) (Miyoshi et al., 2021). Fv sequences of V302A, S66B, and 11G9 (Figure S1A) were acquired from our custom-made hybridoma cell lines (Miyoshi et al., 2021). We constructed "Fv-EGFP" by fusing EGFP to the heavy chain of Fv-clasp and purified the expressed fusion protein from the supernatant of HEK293 cell culture (Figures 1A and 1B). All Fv-EGFPs recognized the relevant expressed epitope-tagged actin in *Xenopus laevis* XTC cells after fixation (Figure 1C). We determined the dissociation rate (k_{off}) by tracking the single-molecule Fv-EGFP bound to epitope-tagged actin (Figure 1D). The data after normalization for the photobleaching rate of EGFP (Figure S1B) are summarized in Table S1. The k_{off} values are consistent with previous studies (Arimori et al., 2017; Fujii et al., 2014; Miyoshi et al., 2021).

Identification of candidate mutation sites in Fv to generate IRIS probes

To achieve high-fidelity IRIS imaging of intracellular proteins (typically, up to 10^4 molecules/μm^2), probes that dissociate in a few seconds are desirable. We therefore sought to increase the dissociation rate of P20.1, 12CA5, 2H8, V302A, and S66B by site-directed mutagenesis. We premised our strategy on the notion that candidate sites for mutagenesis should be commonly conserved in antibodies and would minimally impact specificity. We analyzed 169 open-source Fv sequences and calculated the frequency of amino acids at each position in the alignment of the Chothia numbering scheme (Figure S2) (Chothia and Lesk, 1987). The frequency was consistent with the ranking in a previous study (Li et al., 2019). We selected seven conserved sites at the boundary of CDR and FR, namely H27, H32, H59, H102, L32, L49, and L96 (Figures 2A and S2). The amino acids at these sites are often tyrosine (Y) residues, which play dominant roles in mediating molecular contacts by forming non-polar, hydrogen-bonding, and cation-π interactions (Koide and Sidhu, 2009). Although tyrosine in the middle of CDRs is important for the antigen-antibody interaction (Tsumoto et al., 1995), these seven residues are located at the base of CDR loops (Figure 2B) and do not contact with antigens in many cases (Sela-Culang et al., 2013). Thus, we hypothesized that mutagenesis in these positions might affect the dissociation rate of antibodies without a significant sacrifice of specificity. In addition, H28 at the base of the HCDR1 loop was included among candidate sites. H28 is a conserved site that is often occupied by threonine (T) or serine (S).

To investigate which amino acid substitution could effectively increase the dissociation rate, three candidate sites (H27, H59, and H102) at the base of each HCDR were selected for trial experiment. We performed site-directed mutagenesis on P20.1 Fv-EGFP by substituting each tyrosine residue for each of the other 19 amino acids (Figure 2C). Almost all mutants specifically recognized TARGET-tagged actin expressed in XTC cells, except for HY102P and HY27K. Glycine substitution most effectively accelerated the k_{off}. We therefore selected glycine (G) and alanine (A) as substitution residues. The k_{off} of P20.1 Fv-EGFP with HY59G point mutation ($P20.1^{H1L0}$) was increased by 9-fold (Figure 2D), and the mutant was used in subsequent IRIS imaging with the TARGET tag.

As for the other four Fv-EGFPs, we combined several single point mutations in candidate sites (Table S2). In the case of S66B, the k_{off} of $S66B^{H1L0}$ was doubled to 0.276 s^{-1} by introducing HS28A point mutation (Figure 2E). HY32A, LY96A, and LY32A point mutations in $12CA5^{H5L0}$, $2H8^{H0L3}$, and $V302A^{H0L1}$, respectively, increased the k_{off} by more than one order of

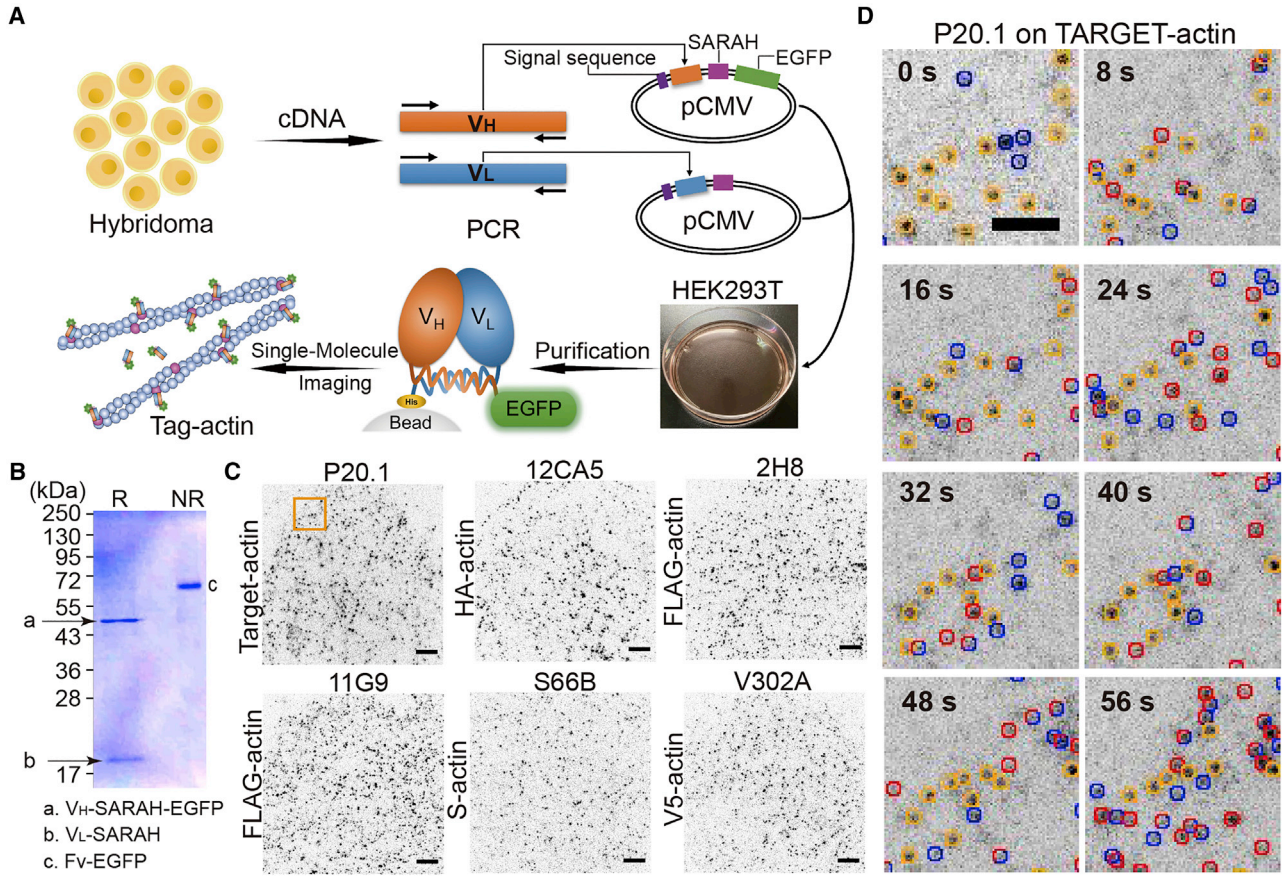

Figure 1. Production of EGFP conjugated Fv-clasps

(A) Diagram of Fv-EGFP generation.

(B) The SDS-PAGE profile of the purified P20.1 (anti-TARGET tag) Fv-EGFP under reducing (R) and non-reducing (NR) conditions. For the reducing condition, the sample was treated with 2% 2-mercaptoethanol and heated at 95°C for 2 min.

(C) Single-molecule imaging of Fv-EGFPs (wild type [WT]) bound to the corresponding epitope-tagged actin expressed in XTC cells. The probes were applied at a very low concentration (0.05–0.1 nM) to perform the single-molecule imaging. Lookup table (LUT) of single-molecule images was inversed in this paper. Scale bar, 5 μm.

(D) Time-lapse images of bound P20.1 Fv-EGFP (corresponds to the yellow box in C) acquired for k_{off} measurement. Bound molecules are indicated by circles in red (new binding), blue (disappears in the next frame), and orange (remains bound). Molecules bound for only one frame are indicated by circles composed of red and blue that are half red and half blue. Exposure time was 300 ms. Scale bar, 2.5 μm.

magnitude (Table S2). To further increase their respective dissociation rate, we sequentially introduced multiple mutations. The k_{off} values of $2H8^{H1L3}$ and $V302A^{H2L1}$ double mutants were increased by 50- and 17-fold compared with wild type (Figure 2E). We also increased the k_{off} of 12CA5 by adding two mutations in $12CA5^{H5L0}$. The k_{off} of $12CA5^{H6L2}$ was 0.601 s^{-1}, which is 2 orders of magnitude faster than wild type (Figures 2D and 2E). Our mutagenesis strategy thus successfully increased the dissociation rate of antibody-based recombinant fluorescent probes.

Generation of IRIS probes based on nanobodies

We also applied the same strategy to a single-domain antibody (nanobody), which consists of only a monomeric variable domain. We analyzed 100 open-source nanobody sequences and calculated the frequency of amino acids at each site (Figure S3A) by aligning them with the Chothia numbering scheme (Sircar et al., 2011). The frequency of amino acids at the candidate sites in nanobodies is similar to that in antibody V_H (Figure S3B). We also noticed that the 37th amino acid (Nb37) in the vicinity of CDR1 is a conserved site occupied by Phe or Tyr, which is different from the corresponding position in V_H (Figure S3B), as described previously (Sircar et al., 2011). We included Nb37 among the candidate sites for mutagenesis of the nanobody in addition to Nb27, Nb28, Nb32, Nb59, and Nb102 (Figure 3A).

We obtained three nanobodies from previous studies, namely NbALFA (anti-ALFA tag) (Götzke et al., 2019), HS69 (anti-Homer) (Dong et al., 2019), and NV-Nb9 (anti-VGLUT) (Schenck et al., 2017). We fused EGFP to the C terminus of the nanobody (hereafter called Nb-EGFP) and purified it from the supernatants of transfected HEK293T cell cultures (Figure S3C). Their k_{off} values were characterized using XTC cells overexpressing ALFA-tagged actin, mCherry-Homer1, and mCherry-VGLUT1. We

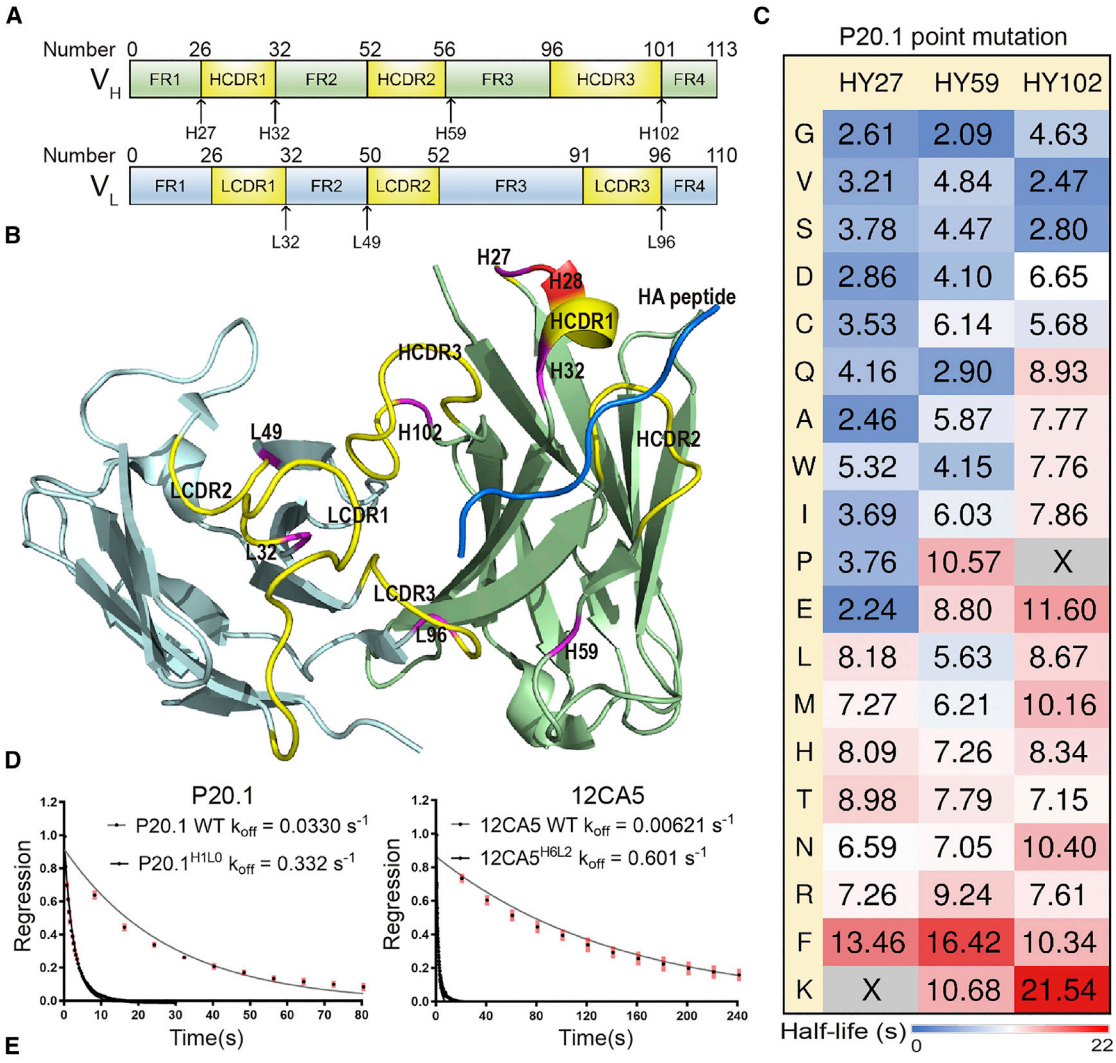

E

IRIS probe (Clone$^{\text{mutant code}}$)	Epitope tag	Mutation site 1	Mutation site 2	Mutation site 3	Mutant koff (1/s)	Mutant half-life (s)	WT half-life (s)
P20.1^{H1L0}	TARGET	HY59G			0.332	2.09	21.0
12CA5^{H6L2}	HA	HT28A	HY32A	LY49A	0.601	1.15	112
2H8^{H1L3}	FLAG	HS28A	LY96A		0.407	1.70	91.1
V302A^{H2L1}	V5	HY27G	LY32A		0.567	1.22	21.5
S66B^{H1L0}	S	HS28A			0.276	2.51	4.97

Figure 2. Increasing the dissociation rate of Fv-EGFPs by mutagenesis

(A) Schematic diagram of candidate sites in Fv. Positions and CDRs are defined by the Chothia numbering scheme.

(B) Candidate sites (red and magenta) at the boundary of CDR and FR, as positioned in the crystal structure of the 12CA5 Fv-clasp (PDB: 5XCU), with a ribbon diagram presentation. V_H, V_L, and CDRs are highlighted in the same colors as in (A).

(C) Half-lives ($T_{1/2} = \ln 2/k_{off}$) of P20.1 Fv-EGFP (anti-TARGET tag) single-point mutants at the base of HCDR1 (HY27), HCDR2 (HY59), and HCDR3 (HY102). Original tyrosine residues were substituted with all other 19 amino acids. Mutants that did not recognize TARGET-actin expressed in XTC cells are annotated in gray (HY27K and HY102P).

(D) Dissociation rate (k_{off}) of P20.1 and 12CA5 determined by analyzing time-lapse images. Normalized regression of tracked molecules (mean value) was fit to a one-phase decay model (n = 3). Standard deviations (SDs) are shown by red bars. See Tables S1 and S3 for more information on fitting parameters.

(E) Summary of mutation sites and dissociation rates of mutant Fv-EGFPs.

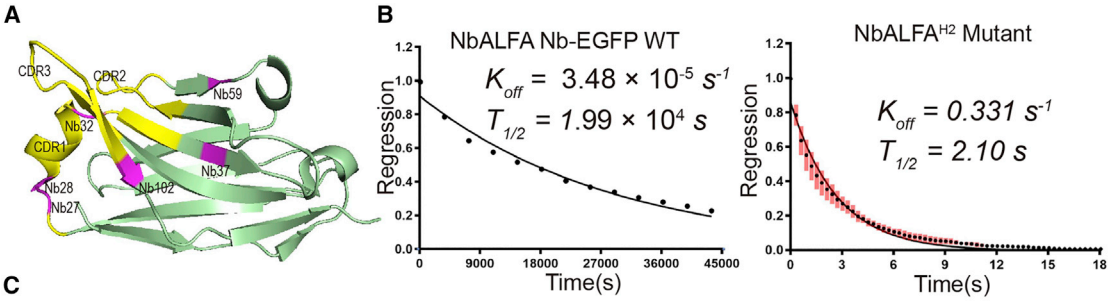

C

IRIS probe (Clone$^{\text{mutant code}}$)	Antigen	Mutation site 1	Mutation site 2	Mutation site 3	Mutation site 4	Mutation site 5	Mutation site 6	Mutant Half-life (s)	Mutant k_{off} (1/s)	WT k_{off} (1/s)
NbALFA^{H2}	ALFA tag	V27G	T28A	Y37A	E53A	R60A	V99A	2.10	3.31 × 10^{-1}	<3.48 × 10^{-5}
HS69^{H3}	Homer	S27G	T28A	F37A	Y59A			7.13	9.71 × 10^{-2}	8.97 × 10^{-4}
NV-Nb9^{H4}	VGLUT	R27G	T28A	Y32A	F37A	Y102A		7.14	9.32 × 10^{-2}	1.64 × 10^{-3}

Figure 3. Generation of fast-dissociating nanobody probes

(A) Candidate sites for mutagenesis of nanobody probes, as represented in the structure of NbALFA (PDB: 6I2G). CDRs are highlighted in yellow. Candidate sites are colored in magenta.

(B) The k_{off} values of NbALFA WT and NbALFAH2 using XTC cells expressing ALFA-actin. See Figure S3E for the time traces of photon counts. See Tables S1 and S3 for more fitting information.

(C) Summary of mutation sites and dissociation rates of nanobody probes. k_{off} values were determined using transfected XTC cells.

mutated several candidate sites of HS69 and NV-Nb9 and increased their k_{off} by two orders of magnitude (Figure S3D). Since the dissociation half-life of NbALFA is longer than 5.5 h (Figure 3B), three alanine mutations at E53, R60, and V99 were first introduced to abolish several interactions with the ALFA tag, according to a previous study (Götzke et al., 2019). The k_{off} of this triple mutant (NbALFA^{H1}) increased to 2.02 × 10^{-3} s^{-1} (Table S2). Three additional point mutations at candidate sites further increased the k_{off} to 0.331 s^{-1} (Figures 3B and 3C). The new candidate site Nb37A proved useful to increase the k_{off} in HS69 and NV-Nb9 (Table S2). We also evaluated the k_{off} of HS69^{H3} and NV-Nb9^{H4} probe using primary cultured neurons. These probes recognized both endogenous targets in neurons and exogenous proteins overexpressed in XTC cells, and the k_{off} was similar in each case (Figure S3D).

Validation of new IRIS probes against epitope tags by super-resolution imaging

We validated the fidelity and specificity of our probes using epitope-tagged actin expressed in XTC cells. In fixed and permeabilized cells, super-resolution images of epitope-tagged actin were reconstructed from single-molecule stacks (Figures 4A, 4G, and 4H). FLAG, TARGET, HA, V5, S, and ALFA probes clearly visualized actin bundles with a resolution of approximately 45 nm in full width at half maximum (FWHM) (Figures 4B and 4C) and resolved two actin bundles 60 nm apart (Figure 4D). The resolution of actin filaments in Figure 4B is estimated to be 52.7 nm using decorrelation analysis (Descloux et al., 2019), which is similar to the FWHM value (45 nm). All five probes recognized the actin filaments of the same distribution and fidelity as the Lifeact probe (Kiuchi et al., 2015) (Figures 4E–4G). We tested the probes at the same concentration using non-transfected XTC cells, as we did in the previous study (Miyoshi et al., 2021), and the binding signal was negligible (Figure S4A). In this study, we quantitively evaluated the non-specific binding and found that the non-specific signal did not increase after mutagenesis at candidate sites (Figures S4A and S4B). Thus, the point mutations at our candidate sites do not impair the specificity of the original antibodies.

Although the probes with a slow dissociation rate could achieve single-molecule imaging at a low concentration, it was difficult to label the target with high fidelity due to insufficient binding frequency within a short timescale (Figure S4C) (Miyoshi et al., 2021). We compared the HA-actin images reconstructed from 30,000 frames using a fast probe (12CA5^{H6L2}, $T_{1/2}$ = 1.15 s) and a slow probe (12CA5^{H4L0}, $T_{1/2}$ = 9.09 s) (Figure S4D). The fast probe could visualize thin HA-actin fibers even in a short imaging period, while the slow probe only sketched the discontinuous actin.

Multiplexed super-resolution imaging of focal adhesions by IRIS probes against epitope tags

To test if our probes can be used for multiplex super-resolution imaging, we simultaneously transfected six epitope-tagged proteins into XTC cells, including V5-actinin, FLAG-vinculin, HA-tagged myosin regulatory light chain 2 (HA-MRLC), TARGET-paxillin, ALFA-zyxin, and S-histone2B (S-H2Bb). The probes were sequentially applied to the transfected, fixed cells in the order of V302A^{H2L1}, Lifeact, 2H8^{H1L3}, P20.1^{H1L0}, 12CA5^{H6L2}, NbALFA^{H2}, and S66B^{H1L0} (Figures 5A and 5B). All probes could be thoroughly washed away in the successive imaging procedure (Figure 5A), and the cross-talk between targets is negligible (Figure S5). In the multiplexed super-resolution image, V302A^{H2L1}, 2H8^{H1L3}, P20.1^{H1L0}, and NbALFA^{H2} probes visualized the thick focal adhesion complex that associates with the tip of actin stress fibers (Figures 5C and 5D). HA-MRLC overlaps with F-actin in the cell center but was not observed near the cell edge (Figure 5B). HA-MRLC is barely

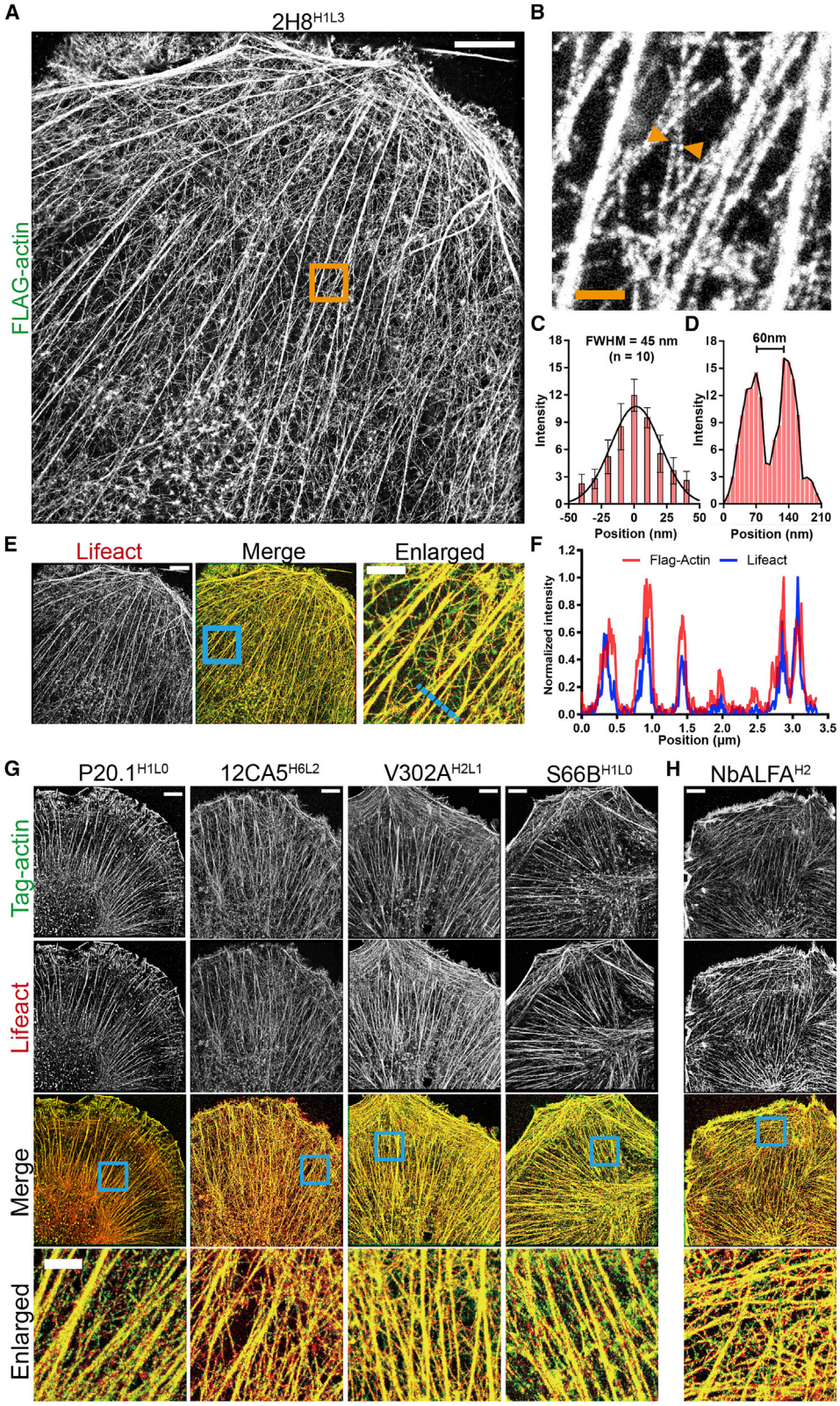

(legend on next page)

colocalized with focal adhesion complexes (Figure 5D), which is consistent with previous immunostaining results (Betapudi, 2010). Moreover, an alternating pattern was visualized between V5-actinin and HA-MRLC along the actin arcs in the lamella of the cell (Figure 5E), as reported in a previous study (Tojkander et al., 2011). This sarcomeric-like organization on arcs is considered to promote actin contraction and shortening (Burnette et al., 2014). In addition, spatially separated clusters of H2B nanodomains inside the cell nucleus were revealed by S66B^{H1L0} probe (Figure 5D), which is in agreement with a previous super-resolution study (Ricci et al., 2015). Therefore, our probes were capable of visualizing multiple epitope-tagged components in a single cell, establishing a proof of principle for multiplexed super-resolution imaging of proteins for which there are no readily available antibodies.

Multiplexed super-resolution imaging of endogenous proteins in neuron

To verify the specificity of IRIS probes against endogenous proteins, we acquired super-resolution images with our new HS69^{H3} and NV-Nb9^{H4} probes in primary cultured neuron. We compared the super-resolved images with the distribution of endogenous proteins. The localization of Homer and VGlut puncta detected by IRIS probes overlapped with the staining pattern of wild-type nanobodies (Dong et al., 2019; Schenck et al., 2017) (Figure S6A). The specificity was also verified by a blank control (Figure S6B) using non-transfected HeLa cells, which express no VGlut and very low levels of Homer (Thul et al., 2017). Moreover, in the neuron expressing mCherry-PSD95, the puncta detected by the HS69^{H3} probe overlapped with the signal for PSD95 (Figure S6C). Pre-synaptic VGlut visualized by the NV-Nb9^{H4} probe showed a clear pairing with dendritic spines marked by Lifeact (Figure S6C). The periodic actin rings along an axon with ~190 nm periodicity (Xu et al., 2013) could be resolved by the Lifeact probe (Figure S6D). These results indicated that our IRIS probes against endogenous targets retained the specificity to identify the correct distribution of proteins at synapses.

We next performed multiplexed super-resolution imaging of endogenous proteins in primary cultured neurons (Figure 6A). In addition to HS69^{H3}, NV-Nb9^{H4}, and Lifeact, we used a new Fv-EGFP derived from an L8/15 antibody against Snapin (Andrews et al., 2019). Snapin is a protein involved in neurotransmission and endosome trafficking (Ilardi et al., 1999; Ye and Cai, 2014). The dissociation rate of wild-type L8/15 is fast enough (0.519 s^{-1}) to be used as an IRIS probe (Table S1). Neurons were infected with adeno-associated virus (AAV-PHP.eB) encoding mCherry cDNA to visualize the morphology of neuron (Figure 6B). Images of four targets were sequentially acquired in the order of F-actin, VGlut, Snapin, and Homer (Figures 6B–6D). We were able to observe clear separation between pre-synaptic VGlut puncta, post-synaptic actin, and the scaffold protein Homer (Figures 6E and S6E). F-actin was highly concentrated at the dendritic spines. Post-synaptic actin was located at the base of Homer-associated structures (Figures 6E and S6E) and occasionally formed a cage-like structure surrounding Homer (Figures 6F and S6E) as described previously (Sidenstein et al., 2016). Snapin distributed ubiquitously in neurons (Figure 6C) and overlapped with VGlut puncta (Figure 6E). The label numbers, which refer to the number of binding (on-off) events of each IRIS probe, of VGlut and Homer puncta in mature synapse are 3,798 ± 945 and 694 ± 269 (mean ± SD), respectively (Figure S6E). The number of VGlut 1/2 and Homer 1b/c molecules in a synapse are reported to be 8,254 (Wilhelm et al., 2014) and 233 (Sugiyama et al., 2005). Based on these numbers, we estimate that approximately 95% of Homer and 37% of VGlut molecules are labeled at least once. Small Homer clusters (~0.1 μm) paired with VGlut are visualized by our probe with 155 labels (Figure 6G).

We next examined whether staining with multiple antibodies might impair the accessibility of another probe in the spines. We compared IRIS images of Homer before and after antibody incubation as schemed in Figure 7A. The label number of Homer probes in each punctum was counted before and after antibody incubation. The targets of primary antibodies are GKAP, SHANK3, and PSD95, which exist in close proximity to Homer (Dani et al., 2010; Tao-Cheng et al., 2015). In the samples that were incubated with both primary antibodies and secondary antibodies, a significant part of signals (~32%) in Homer puncta were lost (Figures 7B and 7C). The label numbers did not decrease in the samples that were incubated only with secondary antibodies (Figures 7B and 7C). These results indicate that interference between antibodies may impair the accessibility of each probe and lead to sparse labeling in conventional multiplexed super-resolution approaches.

In addition, we directly compared IRIS with DNA-based point accumulation for imaging in nanoscale topography (DNA-PAINT) and direct stochastic optical reconstruction microscopy (dSTORM) (van de Linde et al., 2011) by sequentially performing super-resolution imaging on Homer or VGlut in the same neuron samples (Figures S7A and S7B). The synaptic structures have been revealed by localization microscopies (Andreska et al., 2014; Dani et al., 2010; Glebov et al., 2016; Klevanski et al., 2020; Sograte-Idrissi et al., 2020). We compared an IRIS image of synapse (Figure 7B, top left) with published images of

Figure 4. Super-resolution imaging of epitope-tagged actin using mutant probes

(A) Super-resolution images of FLAG-actin expressed in XTC cells using the 2H8^{H1L3}. See Table S4 for imaging parameters. Scale bar, 5 μm.

(B) The enlarged image of the orange box in (A). Decorrelation resolution, 52.7 nm. Scale bar, 500 nm.

(C) Cross-sectional profile of actin bundles (n = 10) aligned by the center of each bundle. The line shows a Gaussian fit with FWHM of 45 nm. Error bars represent SD.

(D) Cross-sectional profiles for two nearby actin bundles between the arrowheads in (B).

(E) Super-resolved actin imaged with Lifeact Atto-488 after washing away the probe in (A). FLAG-actin (green) in (A) and Lifeact image (red) are shown in the merged image. Scale bar, 5 μm for full-scale images and 2.5 μm for the enlarged image.

(F) Cross-sectional profile of actin filaments across the blue dotted line in (E).

(G and H) Comparison of super-resolved actin using other mutant probes (green) and Lifeact (red). The decorrelation resolution of Target-, HA-, V5-, S-, and ALFA-tagged actin is 60.5, 70.9, 75.9, 59.2, and 40.3 nm, respectively. Scale bar, 5 μm for full-scale images and 2.5 μm for enlarged images.

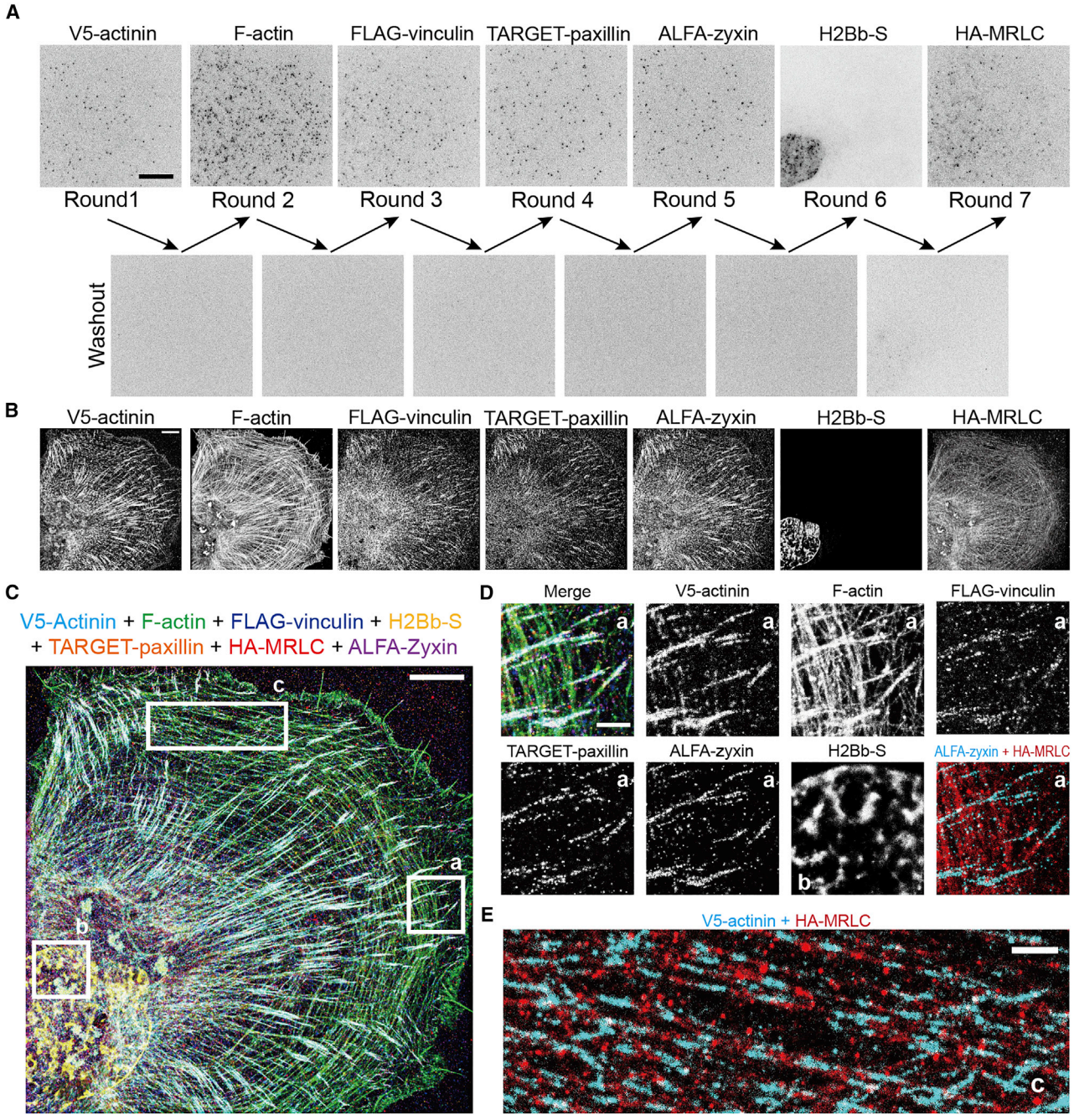

Figure 5. Multiplex super-resolution imaging of the cytoskeleton and focal adhesions in XTC cells

(A) Single-molecule imaging of six epitope-tagged proteins expressed in XTC cells. Image stacks were sequentially acquired using V302A^{H2L1} (2 nM), Lifeact (0.5 nM), 2H8^{H1L3} (2 nM), P20.1^{H1L0} (1.5 nM), NbALFA^{H2} (1 nM), S66B^{H1L0} (1 nM), and 12CA5^{H6L2} (1 nM). Each successive probe was applied to the sample after washing out the preceding probe with PBS. Scale bar, 10 μm.

(B) Super-resolution images were reconstructed from 80,000 frames (V5-actinin), 100,000 frames (F-actin), 60,000 frames (FLAG-vinculin), 60,000 frames (TARGET-paxillin), 60,000 frames (ALFA-zyxin), 24,000 frames (H2Bb-S), and 160,000 frames (HA-MRLC) of single-molecule images. Scale bar, 5 μm.

(C) Seven-color IRIS image of six epitope-tagged proteins and endogenous F-actin in a single XTC cell. Scale bar, 5 μm.

(D) The enlarged images of boxed regions (a) and (b) in (C). Scale bar, 1 μm.

(E) The enlarged images of V5-actinin (cyan) and HA-MRLC (red) along actin arcs in the lamella region (box c) in (C). Scale bar, 1 μm.

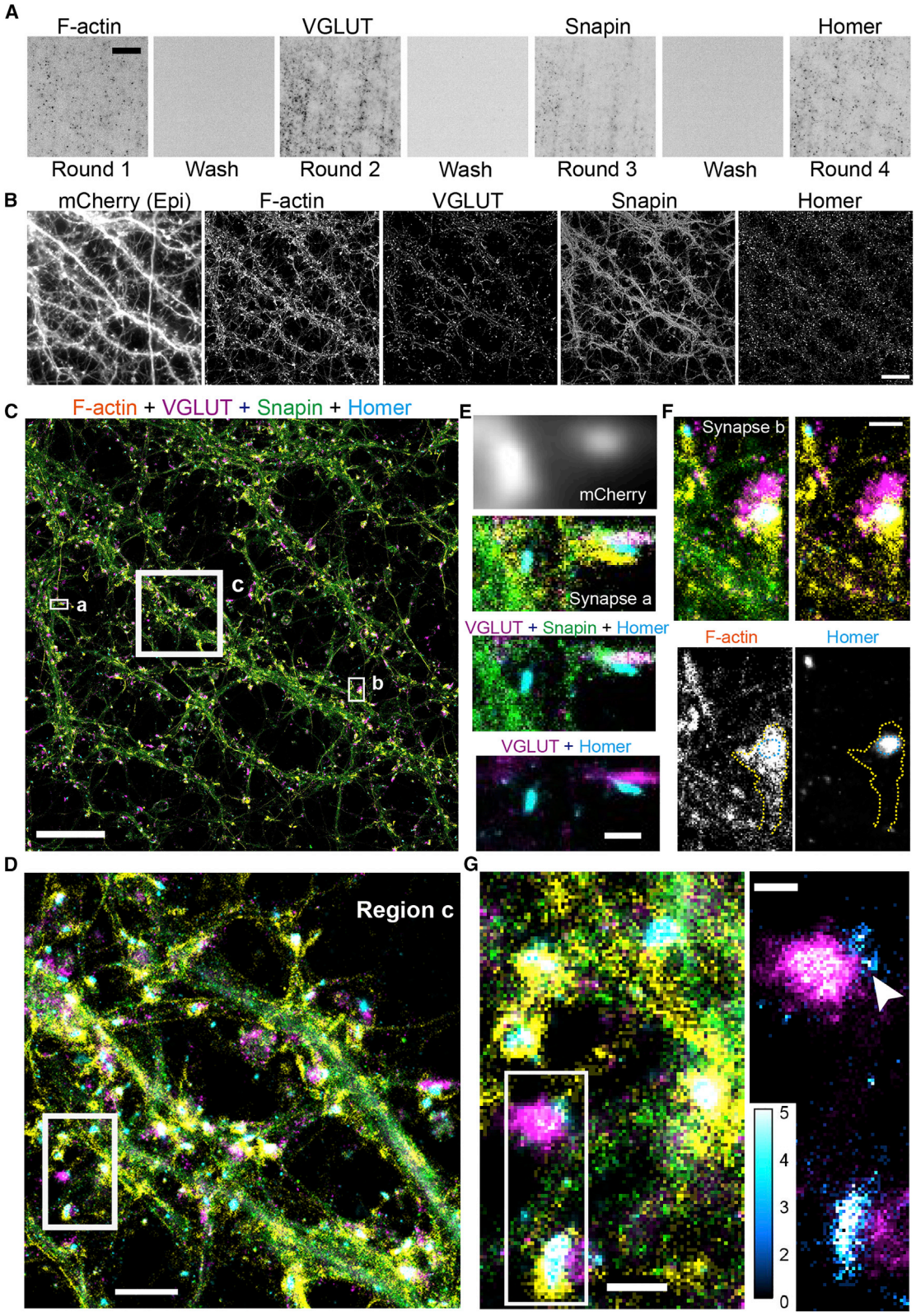

(legend on next page)

STORM (Dani et al., 2010) and DNA-PAINT (Sograte-Idrissi et al., 2020) (Figure S7C). Although we cannot assert which pattern reflects the real distribution of the molecules, IRIS appears to show more continuous labeling than other methods. We further compared the label density and distribution between IRIS and STORM images according to the previous method (Dani et al., 2010). IRIS achieved ~4-fold higher label density than STORM (Figure S7D). Importantly, multiple localization points may arise from repeated detection of a single label in STORM and DNA-PAINT. IRIS probes generated by our approach have the potential to super-resolve multiple endogenous targets of interest with high labeling density.

DISCUSSION

In this study, we discovered a set of common candidate sites in antibody sequences that are amenable to site-directed mutagenesis to increase the dissociation rate, regardless of whether the structure is known. Using alanine or glycine substitutions at candidate sites, we obtained recombinant antibody-based IRIS probes for eight targets, including six epitope tags and two neuronal proteins. As of January 2022, there are 5,746 antibodies available in PDB (Dunbar et al., 2014) with structure information and 23,013 sequenced antibodies in ABCD database (Lima et al., 2020). Based on the sequence information in the antibody database or antibody-producing cell lines, a large repertoire of proteins can be subjected to analysis using IRIS multiplex super-resolution microscopy. As a practical consideration, we use alanine substitution primarily because mutants with glycine substitutions at the same candidate sites sometimes deteriorate the antigen recognition (Table S2). Among the IRIS probes generated in this study, point mutations at H/Nb27G, H/Nb28A, and Nb37A could be frequently introduced without disrupting antigen recognition. Mutations at H/Nb32, H/Nb59, L32, L49, and L96 occasionally led to the loss of antigen recognition, although the k_{off} value could be effectively increased by mutating these sites in most cases. H/Nb102 may be less effective than the other sites in increasing the k_{off}. Combination of point mutations further increases the dissociation rate and retains the binding specificity with a high probability. Multiple point mutations can be introduced collectively to improve the efficiency. We spent typically 2–4 weeks generating a new IRIS probe from an existing antibody sequence.

Most studies aiming to engineer the affinity of antibodies have focused the mutagenesis on the binding interface or CDR loops. Point mutations in the middle of CDRs often lead to the loss of antigen recognition rather than reducing the affinity (Clark et al., 2006; Tanaka et al., 2021; Yamashita et al., 2019). Due to the high diversity of the CDR sequences, mutation sites for each antibody have to be explored individually when no structure information is available. On the other hand, our candidate sites are conserved in most antibodies. Alanine or glycine substitution at the candidate sites could effectively increase the dissociation rate of antibodies. IRIS probes generated by our mutagenesis strategy still retain their specificity, probably because the mutation sites do not contact with the antigens in many cases and the paratope have been well preserved. In the structures of P20.1 Fv-clasp, 12CA5 Fv-clasp, and NbALFA nanobody (Arimori et al., 2017; Götzke et al., 2019), we found that HCDR3 is surrounded by seven candidate sites, namely H27, H28, H32, H102 L32, L49, and L96 (Figure S1C). These amino acids are frequently in contact with a CDR residue (Haidar et al., 2012). Bulky residues at these positions might affect the affinity by modulating the flexibility of CDR loops and shaping them to the right conformation.

We validated the specificity of the mutant probes by comparing the super-resolution images with a positive marker or the staining pattern of the original antibody fragments. Specificity of the probes was also benchmarked by the densities of non-specific binding in non-transfected cell controls (typically ~1% of the total signal in transfected cells). Our quantitative assessment based on single-molecule binding enabled us to validate the specificity of low-affinity binders. Moreover, during the validation process, recombinant fluorescent probes have an advantage over our previous Fab-based probes (Miyoshi et al., 2021). Conjugation of a fluorescent dye to the paratopes may interfere with the antigen-binding capability. We therefore employed labeling by genetically fusing EGFP to recombinant antibody fragments. The use of site-specific chemical labeling methods such as sortagging (Popp et al., 2007) may further improve our fast-dissociating recombinant antibodies by coupling more photostable and brighter organic fluorophores.

IRIS, Exchange-PAINT (Agasti et al., 2017; Guo et al., 2019; Jungmann et al., 2014; Klevanski et al., 2020), and sequential elution-staining STORM (maS^{3}TORM) (Klevanski et al., 2020) could achieve highly multiplexed protein visualization in a single specimen. They use probes with an identical fluorophore, which prevents chromatic aberration. MaS^{3}TORM exchanges the antibodies by harsh elution (0.1% SDS [pH 13], 15 min) and bleaching steps, which might do cumulative damage to the biological sample across multiple rounds of labeling (Klevanski et al., 2020). By

Figure 6. Multiplex super-resolution imaging of synapses in primary cultured neurons

(A) Sequential single-molecule imaging of endogenous neuronal proteins. Images were acquired using Lifeact, NV-Nb9^{H4}, WT L8/15 Fv-EGFP, and HS69^{H3}. The sample was washed 8 times with PBS between successive probes. See Table S4 for imaging parameters. Scale bar, 15 μm.

(B) Super-resolution images of F-actin (Lifeact), VGlut, Snapin, and Homer in primary cultured neurons, reconstructed from single-molecule images in (A). An overall image of the neuron was acquired using overexpressed free mCherry by epi-fluorescence. The decorrelation resolution of F-actin, VGlut, Snapin, and Homer is 77.7, 54.3, 112.0, and 50.9 nm, respectively. Scale bars, 10 μm.

(C) Multiplex imaging, merging four super-resolution images in (B). Scale bars, 10 μm.

(D) Enlarged images of boxed region (c) in (C). Scale bars, 2 μm.

(E and F) Enlarged images of boxed synapses (a) and (b) in (C). Yellow and cyan dotted lines show the shape of the spine and the position of the Homer, respectively. Scale bars, 500 nm.

(G) Enlarged images of boxed region in (D). A small homer cluster (~0.1 μm) was indicated by the white arrowhead in the right panel with 155 labels (see STAR Methods for calculation of label number). Only VGlut (magenta hot) and Homer (cyan hot) clusters are shown in the right panel. Calibration bar shows the number of labels in each pixel (13.5 nm in length). Scale bars, 500 nm (left panel) and 200 nm (right panel).

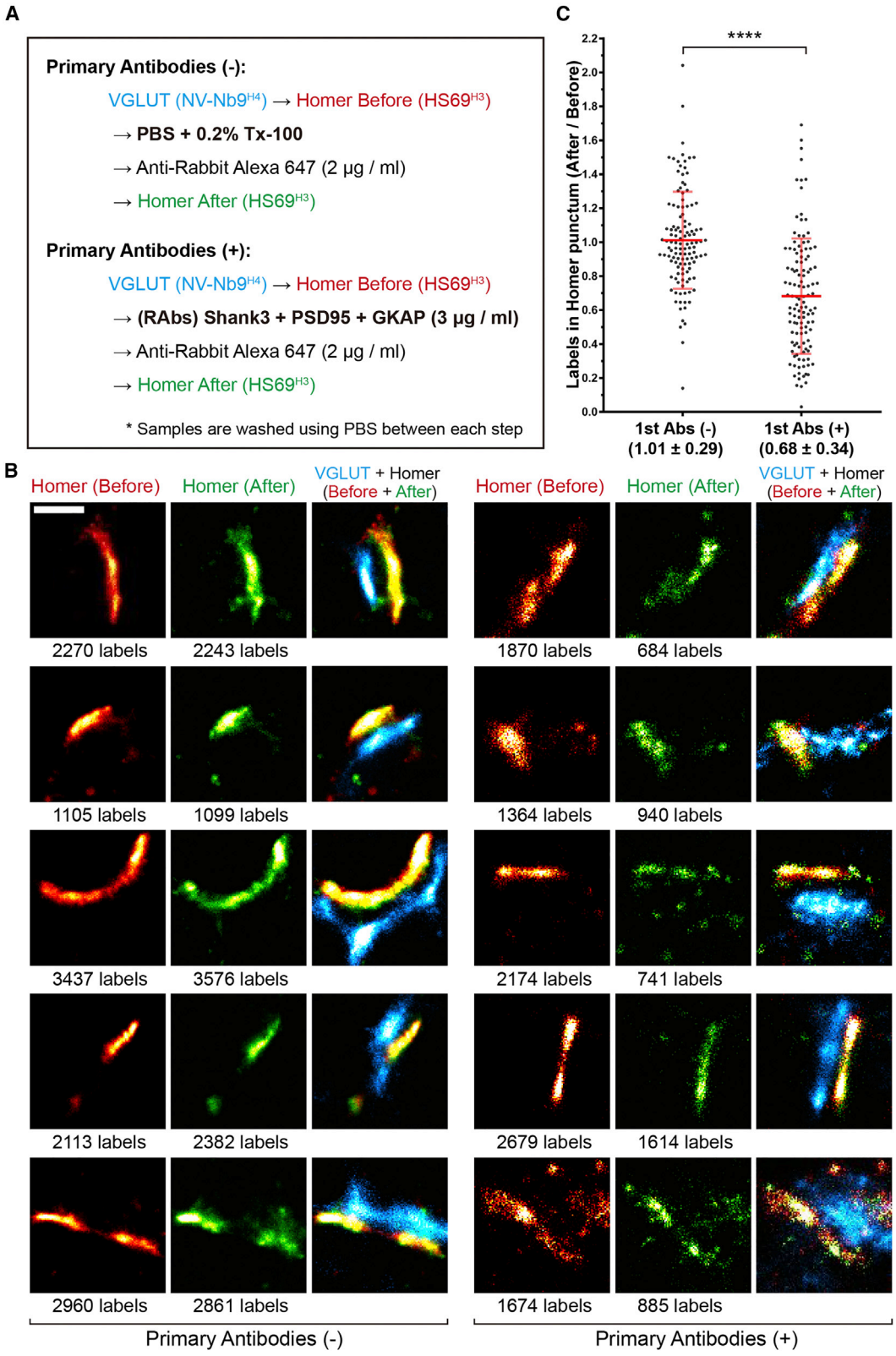

(legend on next page)

contrast, fluorescent probes in IRIS and Exchange-PAINT could be removed by several times of gentle washing. The sample preparation of IRIS is simpler than DNA-PAINT and STORM because IRIS does not require the step of antibody incubation. IRIS and DNA-PAINT do not suffer from photobleaching. This enables longer imaging duration and thus could achieve higher resolution. On the other hand, compared with STORM employing ready-to-use commercial antibodies, IRIS and DNA-PAINT require preparation of individual probes. In addition, it has been reported that chaotropic reagent KSCN can increase the dissociation rate of 12CA5 antibody by several folds (Gunasekara et al., 2021). However, the half-life of 12CA5 on 3×HA tag decreases only to 4.8 min. Importantly, IRIS could overcome the interference between multiple antibodies in a confined area and the resultant scarce labeling, which has been an intrinsic problem of super-resolution microscopy (Huang et al., 2009; Kiuchi et al., 2015).

In summary, we have developed a versatile site-directed mutagenesis strategy to accelerate the dissociation rate of antibodies and generate a series of validated fast-dissociating antibody fragments. These recombinant fragments are especially suited for multitarget super-resolution imaging. Potential applications of these fragments also include multiplexed immunostaining, cell typing/sorting, western blotting, and so on. The pipeline we established can be used in generating fast-dissociating antibodies efficiently from numerous resources of off-the-shelf antibodies.

Limitations of the study

While we established a generalized strategy to accelerate the dissociation rate of existing antibodies by site-directed mutagenesis, the dissociation rate of mutants increased by ~100-fold in this study. For high-affinity antibodies with k_{off} smaller than 10^{-4} s^{-1}, such as NbALFA, it might be necessary to modify additional antigen-binding sites in the middle of CDR loops to further increase the dissociation rate, which would require the information of cocrystal structures. Although the database for antibodies is expanding rapidly, the sequence information of existing antibodies is not always disclosed, making it difficult to develop recombinant IRIS probes for the targets without available antibody sequences. In addition, when using the IRIS probes against epitope tags, the expression level of targets must be estimated empirically by acquiring 1,000–2,000 frames.

STAR★METHODS

Detailed methods are provided in the online version of this paper and include the following:

- KEY RESOURCES TABLE
- RESOURCE AVAILABILITY
  - Lead contact
  - Materials availability
  - Data and code availability
- EXPERIMENTAL MODEL AND SUBJECT DETAILS
  - Cell culture and transfection
  - Primary culture of neurons
- METHOD DETAILS
  - Construction of plasmids
  - AAV production and purification
  - Antibody sequence alignment
  - Purification of recombinant antibody fragments in mammalian cells
  - Measurement of dissociation rate by single-molecule microscopy
  - Super-resolution microscopy
- QUANTIFICATION AND STATISTICAL ANALYSIS

SUPPLEMENTAL INFORMATION

Supplemental information can be found online at https://doi.org/10.1016/j.crmeth.2022.100301.

ACKNOWLEDGMENTS

We thank Sawako Yamashiro (Kyoto University) for providing cDNAs encoding vinculin, paxillin, and zyxin. This work was supported by CREST grant number JPMJCR15G5 to N.W., JSPS KAKENHI grant number 22H00456 to N.W., JSPS KAKENHI grant number 21K06168 to T.K., JSPS KAKENHI grant number 19H04961 to T.K., and BINDS from Japan AMED under grant number 21am0101075 to J.T. Q.Z. was a recipient of Special Research Fellowship from Kobayashi Foundation.

AUTHOR CONTRIBUTIONS

Q.Z., A.M., T.A., and N.W. designed experiments and wrote the manuscript. N.W. and J.T. supervised the project. Q.Z., A.M., S.W., M.T., and T.K. conducted experiments. Q.Z., A.M., and M.S. analyzed the data.

DECLARATION OF INTERESTS

Q.Z., A.M., and N.W. are inventors of a pending patent related to the antibody engineering technology submitted by Kyoto University to Japan Patent Office.

Received: February 11, 2022
Revised: July 7, 2022
Accepted: August 31, 2022
Published: September 20, 2022

REFERENCES

Agasti, S.S., Wang, Y., Schueder, F., Sukumar, A., Jungmann, R., and Yin, P. (2017). DNA-barcoded labeling probes for highly multiplexed exchange-PAINT imaging. Chem. Sci. *8*, 3080–3091. https://doi.org/10.1039/c6sc05420j.

Figure 7. Impact of the spatial interference effect on labeling ratio

(A) Design of the experiment to examine the spatial interference of antibodies inside the post-synaptic region. The antibody incubation time is 90 min for primary antibodies and 60 min for secondary antibodies.

(B) Representative IRIS super-resolution images of VGlut and Homer puncta in the experiment described in (A). Imaging parameters of the Homer (see Table S4) are the same before and after the antibody incubation. The label number of Homer probes is shown at the bottom of each image. Scale bars, 500 nm.

(C) The ratio of Homer labels after and before antibody incubation at each punctum. The data are from 120 puncta in 3 experiments, days *in* vitro 21–24 (DIV21–24) for primary antibodies (−), and 120 puncta in 4 experiments, DIV21–28 for primary antibodies (+). The label ratio of Homer puncta in primary antibodies incubated samples are significantly lower than the primary antibody free samples (unpaired two-tailed t test, ****$p < 0.0001$). Red bars show the mean ± SD.

Al-Lazikani, B., Lesk, A.M., and Chothia, C. (1997). Standard conformations for the canonical structures of immunoglobulins. J. Mol. Biol. *273*, 927–948. https://doi.org/10.1006/jmbi.1997.1354.

Andreska, T., Aufmkolk, S., Sauer, M., and Blum, R. (2014). High abundance of BDNF within glutamatergic presynapses of cultured hippocampal neurons. Front. Cell. Neurosci. *8*, 107. https://doi.org/10.3389/fncel.2014.00107.

Andrews, N.P., Boeckman, J.X., Manning, C.F., Nguyen, J.T., Bechtold, H., Dumitras, C., Gong, B., Nguyen, K., van der List, D., Murray, K.D., et al. (2019). A toolbox of IgG subclass-switched recombinant monoclonal antibodies for enhanced multiplex immunolabeling of brain. Elife *8*, e43322. https://doi.org/10.7554/eLife.43322.

Arimori, T., Kitago, Y., Umitsu, M., Fujii, Y., Asaki, R., Tamura-Kawakami, K., and Takagi, J. (2017). Fv-clasp: an artificially designed small antibody fragment with improved production compatibility, stability, and crystallizability. Structure *25*, 1611–1622.e4. https://doi.org/10.1016/j.str.2017.08.011.

Betapudi, V. (2010). Myosin II motor proteins with different functions determine the fate of lamellipodia extension during cell spreading. PLoS One *5*, e8560. https://doi.org/10.1371/journal.pone.0008560.

Blumhardt, P., Stein, J., Mücksch, J., Stehr, F., Bauer, J., Jungmann, R., and Schwille, P. (2018). Photo-induced depletion of binding sites in DNA-PAINT microscopy. Molecules *23*, E3165. https://doi.org/10.3390/molecules23123165.

Burnette, D.T., Shao, L., Ott, C., Pasapera, A.M., Fischer, R.S., Baird, M.A., Der Loughian, C., Delanoe-Ayari, H., Paszek, M.J., Davidson, M.W., et al. (2014). A contractile and counterbalancing adhesion system controls the 3D shape of crawling cells. J. Cell Biol. *205*, 83–96. https://doi.org/10.1083/jcb.201311104.

Chan, K.Y., Jang, M.J., Yoo, B.B., Greenbaum, A., Ravi, N., Wu, W.L., Sánchez-Guardado, L., Lois, C., Mazmanian, S.K., Deverman, B.E., and Gradinaru, V. (2017). Engineered AAVs for efficient noninvasive gene delivery to the central and peripheral nervous systems. Nat. Neurosci. *20*, 1172–1179. https://doi.org/10.1038/nn.4593.

Chen, S., Weitemier, A.Z., Zeng, X., He, L., Wang, X., Tao, Y., Huang, A.J.Y., Hashimotodani, Y., Kano, M., Iwasaki, H., et al. (2018). Near-infrared deep brain stimulation via upconversion nanoparticle-mediated optogenetics. Science *359*, 679–684. https://doi.org/10.1126/science.aaq1144.

Chothia, C., and Lesk, A.M. (1987). Canonical structures for the hypervariable regions of immunoglobulins. J. Mol. Biol. *196*, 901–917. https://doi.org/10.1016/0022-2836(87)90412-8.

Clark, L.A., Boriack-Sjodin, P.A., Eldredge, J., Fitch, C., Friedman, B., Hanf, K.J.M., Jarpe, M., Liparoto, S.F., Li, Y., Lugovskoy, A., et al. (2006). Affinity enhancement of an in vivo matured therapeutic antibody using structure-based computational design. Protein Sci. *15*, 949–960. https://doi.org/10.1110/ps.052030506.

Dani, A., Huang, B., Bergan, J., Dulac, C., and Zhuang, X. (2010). Superresolution imaging of chemical synapses in the brain. Neuron *68*, 843–856. https://doi.org/10.1016/j.neuron.2010.11.021.

Descloux, A., Grußmayer, K.S., and Radenovic, A. (2019). Parameter-free image resolution estimation based on decorrelation analysis. Nat. Methods *16*, 918–924. https://doi.org/10.1038/s41592-019-0515-7.

Dong, J.X., Lee, Y., Kirmiz, M., Palacio, S., Dumitras, C., Moreno, C.M., Sando, R., Santana, L.F., Südhof, T.C., Gong, B., et al. (2019). A toolbox of nanobodies developed and validated for use as intrabodies and nanoscale immunolabels in mammalian brain neurons. Elife *8*, e48750. https://doi.org/10.7554/eLife.48750.

Dunbar, J., and Deane, C.M. (2016). ANARCI: antigen receptor numbering and receptor classification. Bioinformatics *32*, 298–300. https://doi.org/10.1093/bioinformatics/btv552.

Dunbar, J., Krawczyk, K., Leem, J., Baker, T., Fuchs, A., Georges, G., Shi, J., and Deane, C.M. (2014). SAbDab: the structural antibody database. Nucleic Acids Res. *42*, D1140–D1146. https://doi.org/10.1093/nar/gkt1043.

Eklund, A.S., Ganji, M., Gavins, G., Seitz, O., and Jungmann, R. (2020). Peptide-PAINT super-resolution imaging using transient coiled coil interactions. Nano Lett. *20*, 6732–6737. https://doi.org/10.1021/acs.nanolett.0c02620.

Farrell, M.V., Nunez, A.C., Yang, Z., Pérez-Ferreros, P., Gaus, K., and Goyette, J. (2022). Protein-PAINT: superresolution microscopy with signaling proteins. Sci. Signal. *15*, eabg9782. https://doi.org/10.1126/scisignal.abg9782.

Fujii, Y., Kaneko, M., Neyazaki, M., Nogi, T., Kato, Y., and Takagi, J. (2014). PA tag: a versatile protein tagging system using a super high affinity antibody against a dodecapeptide derived from human podoplanin. Protein Expr. Purif. *95*, 240–247. https://doi.org/10.1016/j.pep.2014.01.009.

Glebov, O.O., Cox, S., Humphreys, L., and Burrone, J. (2016). Neuronal activity controls transsynaptic geometry. Sci. Rep. *6*, 22703. https://doi.org/10.1038/srep22703.

Gunasekara, H., Munaweera, R., and Hu, Y.S. (2021). Chaotropic perturbation of noncovalent interactions of the hemagglutinin tag monoclonal antibody fragment enables superresolution molecular census. ACS Nano *16*, 129–139. https://doi.org/10.1021/acsnano.1c04237.

Guo, S.M., Veneziano, R., Gordonov, S., Li, L., Danielson, E., Perez de Arce, K., Park, D., Kulesa, A.B., Wamhoff, E.C., Blainey, P.C., et al. (2019). Multiplexed and high-throughput neuronal fluorescence imaging with diffusible probes. Nat. Commun. *10*, 4377. https://doi.org/10.1038/s41467-019-12372-6.

Götzke, H., Kilisch, M., Martínez-Carranza, M., Sograte-Idrissi, S., Rajavel, A., Schlichthaerle, T., Engels, N., Jungmann, R., Stenmark, P., Opazo, F., and Frey, S. (2019). The ALFA-tag is a highly versatile tool for nanobody-based bioscience applications. Nat. Commun. *10*, 4403. https://doi.org/10.1038/s41467-019-12301-7.

Haidar, J.N., Yuan, Q.A., Zeng, L., Snavely, M., Luna, X., Zhang, H., Zhu, W., Ludwig, D.L., and Zhu, Z. (2012). A universal combinatorial design of antibody framework to graft distinct CDR sequences: a bioinformatics approach. Proteins *80*, 896–912. https://doi.org/10.1002/prot.23246.

Harris, L.J., Skaletsky, E., and McPherson, A. (1998). Crystallographic structure of an intact IgG1 monoclonal antibody. J. Mol. Biol. *275*, 861–872. https://doi.org/10.1006/jmbi.1997.1508.

Houlihan, G., Gatti-Lafranconi, P., Lowe, D., and Hollfelder, F. (2015). Directed evolution of anti-HER2 DARPins by SNAP display reveals stability/function trade-offs in the selection process. Protein Eng. Des. Sel. *28*, 269–279. https://doi.org/10.1093/protein/gzv029.

Huang, B., Bates, M., and Zhuang, X. (2009). Super-resolution fluorescence microscopy. Annu. Rev. Biochem. *78*, 993–1016. https://doi.org/10.1146/annurev.biochem.77.061906.092014.

Ikeda, K., Koga, T., Sasaki, F., Ueno, A., Saeki, K., Okuno, T., and Yokomizo, T. (2017). Generation and characterization of a human-mouse chimeric high-affinity antibody that detects the DYKDDDDK FLAG peptide. Biochem. Biophys. Res. Commun. *486*, 1077–1082. https://doi.org/10.1016/j.bbrc.2017.03.165.

Ilardi, J.M., Mochida, S., and Sheng, Z.H. (1999). Snapin: a SNARE-associated protein implicated in synaptic transmission. Nat. Neurosci. *2*, 119–124. https://doi.org/10.1038/5673.

Jungmann, R., Avendaño, M.S., Woehrstein, J.B., Dai, M., Shih, W.M., and Yin, P. (2014). Multiplexed 3D cellular super-resolution imaging with DNA-PAINT and Exchange-PAINT. Nat. Methods *11*, 313–318. https://doi.org/10.1038/nmeth.2835.

Kang, T.H., and Seong, B.L. (2020). Solubility, stability, and avidity of recombinant antibody fragments expressed in microorganisms. Front. Microbiol. *11*, 1927. https://doi.org/10.3389/fmicb.2020.01927.

Kiuchi, T., Higuchi, M., Takamura, A., Maruoka, M., and Watanabe, N. (2015). Multitarget super-resolution microscopy with high-density labeling by exchangeable probes. Nat. Methods *12*, 743–746. https://doi.org/10.1038/nmeth.3466.

Klevanski, M., Herrmannsdoerfer, F., Sass, S., Venkataramani, V., Heilemann, M., and Kuner, T. (2020). Automated highly multiplexed super-resolution imaging of protein nano-architecture in cells and tissues. Nat. Commun. *11*, 1552. https://doi.org/10.1038/s41467-020-15362-1.

Koide, S., and Sidhu, S.S. (2009). The importance of being tyrosine: lessons in molecular recognition from minimalist synthetic binding proteins. ACS Chem. Biol. *4*, 325–334. https://doi.org/10.1021/cb800314v.

Lehmann, A., Wixted, J.H.F., Shapovalov, M.V., Roder, H., Dunbrack, R.L., and Robinson, M.K. (2015). Stability engineering of anti-EGFR scFv antibodies by rational design of a lambda-to-kappa swap of the VL framework using a structure-guided approach. mAbs *7*, 1058–1071. https://doi.org/10.1080/19420862.2015.1088618.

Li, L., Chen, S., Miao, Z., Liu, Y., Liu, X., Xiao, Z.X., and Cao, Y. (2019). AbRSA: a robust tool for antibody numbering. Protein Sci. *28*, 1524–1531. https://doi.org/10.1002/pro.3633.

Lima, W.C., Gasteiger, E., Marcatili, P., Duek, P., Bairoch, A., and Cosson, P. (2020). The ABCD database: a repository for chemically defined antibodies. Nucleic Acids Res. *48*, D261–D264. https://doi.org/10.1093/nar/gkz714.

Miyoshi, T., Zhang, Q., Miyake, T., Watanabe, S., Ohnishi, H., Chen, J., Vishwasrao, H.D., Chakraborty, O., Belyantseva, I.A., Perrin, B.J., et al. (2021). Semi-automated single-molecule microscopy screening of fast-dissociating specific antibodies directly from hybridoma cultures. Cell Rep. *34*, 108708. https://doi.org/10.1016/j.celrep.2021.108708.

Oi, C., Gidden, Z., Holyoake, L., Kantelberg, O., Mochrie, S., Horrocks, M.H., and Regan, L. (2020). LIVE-PAINT allows super-resolution microscopy inside living cells using reversible peptide-protein interactions. Commun. Biol. *3*, 458. https://doi.org/10.1038/s42003-020-01188-6.

Olivier, N., Keller, D., Gönczy, P., and Manley, S. (2013). Resolution doubling in 3D-STORM imaging through improved buffers. PLoS One *8*, e69004. https://doi.org/10.1371/journal.pone.0069004.

Pleiner, T., Bates, M., Trakhanov, S., Lee, C.T., Schliep, J.E., Chug, H., Böhning, M., Stark, H., Urlaub, H., and Görlich, D. (2015). Nanobodies: site-specific labeling for super-resolution imaging, rapid epitope-mapping and native protein complex isolation. Elife *4*, e11349. https://doi.org/10.7554/eLife.11349.

Popp, M.W., Antos, J.M., Grotenbreg, G.M., Spooner, E., and Ploegh, H.L. (2007). Sortagging: a versatile method for protein labeling. Nat. Chem. Biol. *3*, 707–708. https://doi.org/10.1038/nchembio.2007.31.

Rabia, L.A., Desai, A.A., Jhajj, H.S., and Tessier, P.M. (2018). Understanding and overcoming trade-offs between antibody affinity, specificity, stability and solubility. Biochem. Eng. J. *137*, 365–374. https://doi.org/10.1016/j.bej.2018.06.003.

Ricci, M.A., Manzo, C., García-Parajo, M.F., Lakadamyali, M., and Cosma, M.P. (2015). Chromatin fibers are formed by heterogeneous groups of nucleosomes in vivo. Cell *160*, 1145–1158. https://doi.org/10.1016/j.cell.2015.01.054.

Schenck, S., Kunz, L., Sahlender, D., Pardon, E., Geertsma, E.R., Savtchouk, I., Suzuki, T., Neldner, Y., Štefanić, S., Steyaert, J., et al. (2017). Generation and characterization of anti-VGLUT nanobodies acting as inhibitors of transport. Biochemistry *56*, 3962–3971. https://doi.org/10.1021/acs.biochem.7b00436.

Schneider, C.A., Rasband, W.S., and Eliceiri, K.W. (2012). NIH Image to ImageJ: 25 years of image analysis. Nat. Methods *9*, 671–675. https://doi.org/10.1038/nmeth.2089.

Sela-Culang, I., Kunik, V., and Ofran, Y. (2013). The structural basis of antibody-antigen recognition. Front. Immunol. *4*, 302. https://doi.org/10.3389/fimmu.2013.00302.

Shi, X., Lim, J., and Ha, T. (2010). Acidification of the oxygen scavenging system in single-molecule fluorescence studies: in situ sensing with a ratiometric dual-emission probe. Anal. Chem. *82*, 6132–6138. https://doi.org/10.1021/ac1008749.

Sidenstein, S.C., D'Este, E., Böhm, M.J., Danzl, J.G., Belov, V.N., and Hell, S.W. (2016). Multicolour multilevel STED nanoscopy of actin/spectrin organization at synapses. Sci. Rep. *6*, 26725. https://doi.org/10.1038/srep26725.

Sircar, A., Sanni, K.A., Shi, J., and Gray, J.J. (2011). Analysis and modeling of the variable region of camelid single-domain antibodies. J. Immunol. *186*, 6357–6367. https://doi.org/10.4049/jimmunol.1100116.

Sograte-Idrissi, S., Schlichthaerle, T., Duque-Afonso, C.J., Alevra, M., Strauss, S., Moser, T., Jungmann, R., Rizzoli, S.O., and Opazo, F. (2020). Circumvention of common labelling artefacts using secondary nanobodies. Nanoscale *12*, 10226–10239. https://doi.org/10.1039/d0nr00227e.

Sugiyama, Y., Kawabata, I., Sobue, K., and Okabe, S. (2005). Determination of absolute protein numbers in single synapses by a GFP-based calibration technique. Nat. Methods *2*, 677–684. https://doi.org/10.1038/nmeth783.

Suzuki, J., Kanemaru, K., Ishii, K., Ohkura, M., Okubo, Y., and Iino, M. (2014). Imaging intraorganellar Ca2+ at subcellular resolution using CEPIA. Nat. Commun. *5*, 4153. https://doi.org/10.1038/ncomms5153.

Tabata, S., Nampo, M., Mihara, E., Tamura-Kawakami, K., Fujii, I., and Takagi, J. (2010). A rapid screening method for cell lines producing singly-tagged recombinant proteins using the "TARGET tag" system. J. Proteomics *73*, 1777–1785. https://doi.org/10.1016/j.jprot.2010.05.012.

Tanaka, T., Thomas, J., Van Montfort, R., Miller, A., and Rabbitts, T. (2021). Pan RAS-binding compounds selected from a chemical library by inhibiting interaction between RAS and a reduced affinity intracellular antibody. Sci. Rep. *11*, 1712. https://doi.org/10.1038/s41598-021-81262-z.

Tao-Cheng, J.H., Azzam, R., Crocker, V., Winters, C.A., and Reese, T. (2015). Depolarization of hippocampal neurons induces formation of nonsynaptic NMDA receptor islands resembling nascent postsynaptic densities. eNeuro *2*, ENEURO.0066-15.2015. https://doi.org/10.1523/ENEURO.0066-15.2015.

Tas, R.P., Albertazzi, L., and Voets, I.K. (2021). Small peptide-protein interaction pair for genetically encoded, fixation compatible peptide-PAINT. Nano Lett. *21*, 9509–9516. https://doi.org/10.1021/acs.nanolett.1c02895.

Thul, P.J., Åkesson, L., Wiking, M., Mahdessian, D., Geladaki, A., Ait Blal, H., Alm, T., Asplund, A., Björk, L., Breckels, L.M., et al. (2017). A subcellular map of the human proteome. Science *356*, eaal3321. https://doi.org/10.1126/science.aal3321.

Tiller, K.E., Li, L., Kumar, S., Julian, M.C., Garde, S., and Tessier, P.M. (2017). Arginine mutations in antibody complementarity-determining regions display context-dependent affinity/specificity trade-offs. J. Biol. Chem. *292*, 16638–16652. https://doi.org/10.1074/jbc.M117.783837.

Tojkander, S., Gateva, G., Schevzov, G., Hotulainen, P., Naumanen, P., Martin, C., Gunning, P.W., and Lappalainen, P. (2011). A molecular pathway for myosin II recruitment to stress fibers. Curr. Biol. *21*, 539–550. https://doi.org/10.1016/j.cub.2011.03.007.

Tsumoto, K., Ogasahara, K., Ueda, Y., Watanabe, K., Yutani, K., and Kumagai, I. (1995). Role of Tyr residues in the contact region of anti-lysozyme monoclonal antibody HyHEL10 for antigen binding. J. Biol. Chem. *270*, 18551–18557. https://doi.org/10.1074/jbc.270.31.18551.

Vallet-Courbin, A., Larivière, M., Hocquellet, A., Hemadou, A., Parimala, S.N., Laroche-Traineau, J., Santarelli, X., Clofent-Sanchez, G., Jacobin-Valat, M.J., and Noubhani, A. (2017). A recombinant human anti-platelet scFv antibody produced in Pichia pastoris for atheroma targeting. PLoS One *12*, e0170305. https://doi.org/10.1371/journal.pone.0170305.

van de Linde, S., Löschberger, A., Klein, T., Heidbreder, M., Wolter, S., Heilemann, M., and Sauer, M. (2011). Direct stochastic optical reconstruction microscopy with standard fluorescent probes. Nat. Protoc. *6*, 991–1009. https://doi.org/10.1038/nprot.2011.336.

Watanabe, N., and Mitchison, T.J. (2002). Single-molecule speckle analysis of actin filament turnover in lamellipodia. Science *295*, 1083–1086. https://doi.org/10.1126/science.1067470.

Watson, J.F., Pinggera, A., Ho, H., and Greger, I.H. (2021). AMPA receptor anchoring at CA1 synapses is determined by N-terminal domain and TARP γ8 interactions. Nat. Commun. *12*, 5083. https://doi.org/10.1038/s41467-021-25281-4.

Wilhelm, B.G., Mandad, S., Truckenbrodt, S., Kröhnert, K., Schäfer, C., Rammner, B., Koo, S.J., Claßen, G.A., Krauss, M., Haucke, V., et al. (2014). Composition of isolated synaptic boutons reveals the amounts of vesicle trafficking proteins. Science *344*, 1023–1028. https://doi.org/10.1126/science.1252884.

Xu, K., Zhong, G., and Zhuang, X. (2013). Actin, spectrin, and associated proteins form a periodic cytoskeletal structure in axons. Science *339*, 452–456. https://doi.org/10.1126/science.1232251.

Yamashiro, S., Mizuno, H., Smith, M.B., Ryan, G.L., Kiuchi, T., Vavylonis, D., and Watanabe, N. (2014). New single-molecule speckle microscopy reveals modification of the retrograde actin flow by focal adhesions at nanometer scales. Mol. Biol. Cell *25*, 1010–1024. https://doi.org/10.1091/mbc.E13-03-0162.

Yamashita, T., Mizohata, E., Nagatoishi, S., Watanabe, T., Nakakido, M., Iwanari, H., Mochizuki, Y., Nakayama, T., Kado, Y., Yokota, Y., et al. (2019). Affinity improvement of a cancer-targeted antibody through alanine-induced adjustment of antigen-antibody interface. Structure *27*, 519–527.e5. https://doi.org/10.1016/j.str.2018.11.002.

Ye, X., and Cai, Q. (2014). Snapin-mediated BACE1 retrograde transport is essential for its degradation in lysosomes and regulation of APP processing in neurons. Cell Rep. *6*, 24–31. https://doi.org/10.1016/j.celrep.2013.12.008.

Zhou, H., Fisher, R.J., and Papas, T.S. (1994). Optimization of primer sequences for mouse scFv repertoire display library construction. Nucleic Acids Res. *22*, 888–889. https://doi.org/10.1093/nar/22.5.888.

Zhou, R., Han, B., Xia, C., and Zhuang, X. (2019). Membrane-associated periodic skeleton is a signaling platform for RTK transactivation in neurons. Science *365*, 929–934. https://doi.org/10.1126/science.aaw5937.

STAR★METHODS

KEY RESOURCES TABLE

REAGENT or RESOURCE	SOURCE	IDENTIFIER
Antibodies		
Rabbit polyclonal anti-HOMER1	Proteintech	Cat#12433-1-AP; RRID: AB_2295573
Rabbit recombinant anti-VGluT1 (clone EPR22269)	Abcam	Cat#ab227805; RRID: AB_2868428
Rabbit monoclonal anti-PSD95 (clone D27E11)	Cell Signaling Technology	Cat#3450; RRID: AB_2292883
Rabbit monoclonal anti-SHANK3 (clone D5K6R)	Cell Signaling Technology	Cat#64555; RRID: AB_2799661
Rabbit polyclonal anti-GKAP	Cell Signaling Technology	Cat#13602; RRID: AB_2798272
Goat Anti-Rabbit IgG H&L (Alexa Fluor 647)	Abcam	Cat#ab150079; RRID: AB_2722623
Bacterial and virus strains		
pAAV-hSyn1-mTurquoise2	Chan et al. (2017)	Addgene plasmid#99125
pAAV-hSyn1-mCherry	This paper	N/A
pAAV-hSyn1-mCherry-PSD95	This paper	N/A
DH5α	TOYOBO Life Science	Cat#DNA-913
Stbl3	Thermo Fisher Scientific	Cat#C737303
Chemicals, peptides, and recombinant proteins		
Imidazole	Nacalai Tesque	Cat#19004-35
Glucose oxidase	Sigma Aldrich	Cat#G2133-50KU
Pyranose oxidase	Sigma Aldrich	Cat#P4234-1KU
Catalase	SERVA	Cat#26910.01
Mercaptoethylamine	Sigma Aldrich	Cat#M6500-25G
See Table S2 for recombinant EGFP-fused Fv-clasps and nanobodies	This paper	N/A
Critical commercial assays		
Massive-AB 2-Plex DNA-PAINT kit	Massive Photonics	N/A
Experimental models: Cell lines		
Xenopus laevis XTC cells	Watanabe and Mitchison (2002)	Watanabe and Mitchison (2002)
HEK293T	ATCC	Cat#CRL-1573; RRID:CVCL_0063
HeLa	ATCC	Cat#CCL2; RRID:CVCL_0030
Custom-made Hybridomas for FLAG-tag (clone 11G9)	Miyoshi et al. (2021)	N/A
Custom-made Hybridomas for V5-tag (clone V302A)	Miyoshi et al. (2021)	N/A
Custom-made Hybridomas for S-tag (clone S66B)	Miyoshi et al. (2021)	N/A
Experimental models: Organisms/strains		
Rat (Slc: Wistar)	Japan SLC, Inc.	RRID: RGD2314928
Oligonucleotides		
Primers for Fv cloning, see Table S5	This paper	N/A
Primers for or site-directed mutagenesis, see Table S6	This paper	N/A
5′-atcaagcttcgatgggggagcaacctatcttc-3′ (Homer1 cloning, forward)	Eurofins	N/A
5′-atcgaattcttagctgcattccagtagcttgg-3′ (Homer1 cloning, reverse)	Eurofins	N/A
5′-atcctcgagctatgttgatcccttcagcagc-3′ (VGLUT1 cloning, forward)	Eurofins	N/A
5′-atcaagctttcagtagtcccggacaggg-3′ (VGLUT1 cloning, reverse)	Eurofins	N/A

(*Continued on next page*)

Continued

REAGENT or RESOURCE	SOURCE	IDENTIFIER
5′-atcctcgagctatggactgtctctgtatagtgac-3′ (PSD95 cloning, forward)	Eurofins	N/A
5′-atcgaattctcagagtctctctcgggct-3′ (PSD95 cloning, reverse)	Eurofins	N/A
Recombinant DNA		
delCMV-EGFP-C1 plasmid vector	Watanabe and Mitchison (2002)	N/A
pEGFP-C1	Clontech Laboratories	Cat#6084-1
pEGFP-N3	Clontech Laboratories	Cat#6080-1
pEGFP-actin	Clontech Laboratories	Cat#6116-1
delCMV-FLAG-C1-actin	This paper	N/A
pTARGET-C1-actin	This paper	N/A
pHA-C1-actin	This paper	N/A
pS-C1-actin	This paper	N/A
pV5-C1-actin	This paper	N/A
pALFA-C1-actin	This paper	N/A
Human histone cluster 1 H2B family member b cDNA	Dharmacon	NM_021062.2
Xenopus laevis paxillin cDNA	Open Biosystems	BC070716.1
Xenopus laevis alpha-actinin cDNA	Open Biosystems	BC043995
Homo sapiens zyxin cDNA	Open Biosystems	BC010031.2
Homo sapiens vinculin cDNA	Yamashiro et al. (2014)	BC039174.1
Xenopus laevis myosin light chain regulatory A cDNA	Eurofins	NM_001086846.1
pV5-C1-actinin	This paper	N/A
pFLAG-C1-vinculin	This paper	N/A
pS-N3-H2Bb	This paper	N/A
pTARGET-C1-paxillin	This paper	N/A
pHA-C1-MRLC	This paper	N/A
pALFA-C1-zyxin	This paper	N/A
Mammalian expression plasmid of anti-Snapin (L8/15R) recombinant mouse monoclonal antibody	Andrews et al. (2019)	Addgene plasmid#140071
Mammalian expression plasmid of anti-TARGET (P20.1) Fv-clasp (v2)	Arimori et al. (2017)	Arimori et al. (2017)
Mammalian expression plasmid of anti-HA (12CA5) Fv-clasp (v2)	Arimori et al. (2017)	Arimori et al. (2017)
Anti-FLAG-2H8 antibody cDNA	Ikeda et al. (2017)	Ikeda et al. (2017)
ALFA-tag binding nanobody (NbALFA)	Götzke et al. (2019)	PDB ID: 6I2G
HS69 anti-Homer1 nanobody	Dong et al. (2019)	Addgene plasmid#134716
Nanobody-anti-VGLUT1-Nb9 (NV-Nb9)	Schenck et al. (2017)	PDB ID: 5OCL
P20.1 Fv-clasp-EGFP-6×His	This paper	N/A
12CA5 Fv-clasp-EGFP-6×His	This paper	N/A
11G9 Fv-clasp-EGFP-6×His	This paper	N/A
2H8 Fv-clasp-EGFP-6×His	This paper	N/A
V302A Fv-clasp-EGFP-6×His	This paper	N/A
S66B Fv-clasp-EGFP-6×His	This paper	N/A
L8/15 Fv-clasp-EGFP-6×His	This paper	N/A
NbALFA Nanobody-EGFP-6×His	This paper	N/A
HS69 Nanobody-EGFP-6×His	This paper	N/A
NV-Nb9 Nanobody-EGFP-6×His	This paper	N/A
See Table S2 for the DNA of antibody mutants	This paper	N/A

(*Continued on next page*)

Continued

REAGENT or RESOURCE	SOURCE	IDENTIFIER
Software and algorithms		
ImageJ	Schneider et al. (2012)	https://imagej.nih.gov/ij/;
Decorrelation analysis algorithm	Descloux et al. (2019)	https://github.com/Ades91/ImDecorr
MetaMorph	Molecular Devices	N/A
GraphPad Prism 7	Dotmatics	https://www.graphpad.com/
Tanitracer	Miyoshi et al. (2021)	https://github.com/takushim/tanitracer
ANARCI	Dunbar and Deane (2016)	http://opig.stats.ox.ac.uk/webapps/newsabdab/sabpred/anarci/
PyMOL	Schrödinger, LLC	https://www.pymol.org/
SnapGene	Dotmatics	https://www.snapgene.com/
Other		
Leibovitz's L-15 Medium (for cell culture)	Thermo Fisher Scientific	Cat#11415-064
Leibovitz's L-15 (phenol red free)	Nacalai Tesque	Custom Synthesis
Value FBS–Brazil	Thermo Fisher Scientific	Cat#10270-106
DMEM	Nacalai Tesque	Cat#08459-35
HBSS	Nacalai Tesque	Cat#17460-15
MEM	Thermo Fisher Scientific	Cat#51200038
Neurobasal™ Medium, minus phenol red	Thermo Fisher Scientific	Cat#12348017
Isoflurane	Pfizer	N/A
Pyruvic acid	Thermo Fisher Scientific	Cat#11360070
MACS NeuroBrew 21	Miltenyi Biotec	Cat#130-093-566
L-Glutamine	Thermo Fisher Scientific	Cat#25030149
2.5 g/L-Trypsin/1 mmol/L-EDTA Solution	Nacalai Tesque	Cat#35554-64
Ni-NTA Agarose	QIAGEN	Cat#30210
AAVanced Concentration Reagent	SBI	Cat#AAV100A-1
Neon™ Transfection System	ThermoFisher Scientific	Cat#MPK5000
Neon™ Transfection System 10 mL Kit	Thermo Fisher SCIENTIFIC	Cat#MPK1096
Envision 2105	PerkinElmer	Cat#2105
BSA	Nacalai Tesque	Cat#01860-65
Lipofectamine 3000 Transfection Reagent	ThermoFisher Scientific	Cat#L3000015
293fectin Transfection Reagent	ThermoFisher Scientific	Cat# 12347500
Bovine fibronectin	Sigma Aldrich	Cat#F1141
IX83 Inverted microscope	Olympus	IX83
Evolve 512 EMCCD camera	Photometrics	Evolve 512
Z Drift Compensator IX3-ZDC2	Olympus	IX3-ZDC2

RESOURCE AVAILABILITY

Lead contact

Further information and requests for resources and reagents should be directed to and will be fulfilled by the lead contact, Naoki Watanabe (watanabe.naoki.4v@kyoto-u.ac.jp).

Materials availability

All materials and constructs used in this study are maintained by Dr. Watanabe's laboratory and are available upon request.

Data and code availability

- All data reported in this paper will be shared by the lead contact upon request.
- This paper does not report original code.
- Any additional information required to reanalyze the data reported in this paper is available from the lead contact upon request.

EXPERIMENTAL MODEL AND SUBJECT DETAILS

Cell culture and transfection

Xenopus laevis XTC cells were cultured in 70% Leibovitz's L15 medium (Thermo Fisher Scientific) supplemented with 10% fetal bovine serum (FBS; Thermo Fisher Scientific) as previously described (Watanabe and Mitchison, 2002). Transfection of XTC cells was performed using the Neon Transfection System (ThermoFisher Scientific) following the manufacturer's protocol. On the next day, transfected cells were trypsinized and maintained in a new flask containing 70% L15 medium with 10% FBS until imaging. HEK293T and Hela cells were maintained in Dulbecco's modified eagle medium (DMEM, high glucose; Nacalai Tesque, Inc) containing 10% FBS.

Primary culture of neurons

Timed pregnant Wistar rats (SHIMIZU Laboratory Supplies) were euthanized by isoflurane (Pfizer) and hippocampi were isolated from the embryos (E20). The sex of embryos and the age of the pregnant rats were not determined. Dissected tissues were digested with 0.25% trypsin-EDTA (Nacalai Tesque, Inc) at 37°C for 5 min and washed with Hanks' Balanced Salt Solution (HBSS; Nacalai Tesque, Inc) three times. Digested tissues were gently suspended in Minimum Essential Medium (MEM; Thermo Fisher Scientific) supplemented with 10 mg/mL pyruvic acid (Nacalai Tesque, Inc), MACS NeuroBrew 21 (Miltenyi Biotec), and 2 mM L-Glutamine (ThermoFisher Scientific). Scattered neurons were then counted and plated onto poly-L-lysine-coated (Sigma) 24-mm coverslips (Matsunami Glass). Culture medium was changed to Neurobasal Medium (ThermoFisher Scientific) supplemented with MACS NeuroBrew 21 and 2 mM L-Glutamine in DIV2. Cells were maintained in a humidified atmosphere of 5% CO_2 at 37°C. Animal experiments were carried out in accordance with the guidelines and protocols approved by Kyoto University. The experiment is approved by Institute of Laboratory Animals, Graduate School of Medicine, Kyoto University (approval number: Medkyo-18046).

METHOD DETAILS

Construction of plasmids

Expression vectors for P20.1 and 12CA5 Fv-clasp (v2) were obtained from a previous study (Arimori et al., 2017). The original signal peptide was replaced with a mouse IgH signal sequence as previously reported (Suzuki et al., 2014). An EGFP cDNA was added to the heavy chain of Fv-clasp between SARAH domain and 6xHis tag by AgeI. Antibody sequences of 11G9, V302A and S66B were cloned from hybridoma cell lines (Miyoshi et al., 2021), using primer sets (Table S5) that were slightly modified, based on a previously described optimization (Zhou et al., 1994). The antibody cDNA of 2H8 (Ikeda et al., 2017), NbALFA (Götzke et al., 2019), HS69 (Dong et al., 2019) and NV-Nb9 (Schenck et al., 2017) were artificially synthesized. Antibody sequence of L8/15 (anti-snapin) was a gift from James Trimmer (Addgene plasmid #140071). We introduced point mutations to antibody fragments using primer sets shown in Table S6.

The expression vectors for XTC cells, pEGFP-C1, pEGFP-actin, were purchased from Clontech. These vectors were used to express epitope-tagged proteins after replacing the EGFP sequences with epitope tags. Cytomegalovirus (CMV) promoter of pFLAG-actin was truncated (delCMV) to lower cytotoxicity (Miyoshi et al., 2021; Watanabe and Mitchison, 2002). cDNAs of human vinculin (GenBank: BC039174) (Yamashiro et al., 2014), *Xenopus laevis* paxillin (GenBank: BC070716), *Xenopus laevis* alpha-actinin (GenBank: BC043995) and human zyxin (GenBank: BC010031) were obtained from Open Biosystems. A cDNA encoding *Xenopus laevis* myosin light chain (GenBank: NM_001086846.1) was artificially synthesized. cDNAs encoding Homer1, VGLUT1 and PSD95 were cloned from a mouse brain cDNA library (Takara-bio) using primer pairs as shown in the key resources table.

A plasmid set (Chan et al., 2017) (pAAV-hSyn1-mTurquoise2; pUCmini-iCAP-PHP.eB; pAdDeltaF6) for AAV production was purchased form Addgene (Plasmid #99125). mTurquoise2 was replaced with mCherry for neuron infection.

AAV production and purification

The adeno-associated virus vectors pAAV-hSyn1-mCherry or pAAV-hSyn1-mCherry-PSD95 were co-transfected with pAdDeltaF6 (helper) and AAV-PHP.eB Cap, which provide AAV with replication protein and capsid protein, respectively, into HEK293FT cells (Invitrogen) using 293fectin transfection reagent (Invitrogen). The supernatant was collected after 72 hours, centrifuged at 1,500 g for 30 minutes and then filtered through a 0.45 μm syringe filter (Sartorius) as described previously (Chen et al., 2018). AAV in the supernatant was precipitated by adding AAVanced Concentration Reagent (SBI) for 24–72 hours. After precipitation, the suspension was centrifuged at 1,500 g for 30 minutes, and the supernatant was removed by aspiration. The pellet was resuspended in phosphate-buffered saline (PBS) and then vortexed.

Antibody sequence alignment

Open-source antibody and nanobody sequences were obtained from PDB. CDRs of antibodies were defined using the Chothia Numbering Scheme (http://www.bioinf.org.uk/abs/chothia.html) (Al-Lazikani et al., 1997). Nanobody sequences were aligned using the ANARCI web server (Dunbar and Deane, 2016) in the Chothia numbering scheme. Nanobody CDRs were defined according to the previously described, using rules based on Chothia numbering (Sircar et al., 2011).

Purification of recombinant antibody fragments in mammalian cells

For the purification of EGFP-conjugated Fv fragments, V_H-SARAH-EGFP and V_L-SARAH were co-transfected into HEK293T cells at a 1 : 1 molar ratio using a Lipofectamine 3000 Transfection Kit (ThermoFisher Scientific). EGFP conjugated nanobodies (Nb-EGFPs) were transfected into HEK293 cells using the same kit. Culture supernatants were collected 4–5 days after the transfection. Antibody fragments in the supernatants were collected with Ni-NTA agarose (QIAGEN) at room temperature for 2 hours, washed three times with ice-cold Tris Buffered Saline (TBS; 20 mM Tris, 150 mM NaCl, pH 7.5) and once with TBS containing 10 mM imidazole (Nacalai Tesque, Inc). Bound antibody fragments were eluted with 200 mM imidazole in TBS. The purified polypeptides were dialyzed vs. TBS using Spectra/por membrane (MWCO: 6–8 kD, Spectrum Laboratories, Inc.), with two exchanges of buffer overnight at 4°C. Transiently transfected HEK293T cells in a 10 cm dish typically yield 0.34–4.02 μg (5–60 pmol) Fv-EGFP and 0.41–4.92 μg (10–120 pmol) Nb-EGFP, which are enough for 20–60 times of IRIS imaging. The purified probes were mostly fluorescent because the concentration measured by fluorescent intensity was comparable to the concentration determined by CBB protein assay.

Measurement of dissociation rate by single-molecule microscopy

XTC cells expressing epitope-tagged actin were spread on coverslips coated with 100 μg/mL poly-L-lysine (Sigma) and 10 μg/mL fibronectin (Sigma) for 1 h to ensure the formation of flat lamellipodia and lamella. Next, the cells were fixed with 3. 7% PFA in cytoskeleton buffer (10 mM MES, 90 mM KCl, 3 mM $MgCl_2$, 2 mM EGTA, pH 6.1) containing 0.5% Triton-X100 (Nacalai tesque) for 20 min, then blocked with 3% BSA (Nacalai tesque) in PBS. Probes were applied at 0.05–0.1 nM in HEPES-KCl-Tx buffer (10 mM HEPES-KOH, 90 mM KCl, 3 mM $MgCl_2$, 0.1 mM dithiothreitol, 0.2% Triton-X100, pH 7.2) with an oxygen scavenging mixture (0.2 mg/mL glucose oxidase, 0.035 mg/mL catalase, 0.45% glucose, 0.5% 2-mercaptoethanol) (Kiuchi et al., 2015).

Time-lapse imaging of single-molecules bound to fixed XTC cells expressing epitope tagged actin or target proteins were acquired under 488-nm illumination with an Olympus IX83 inverted microscope equipped with an IX3-ZDC2 Z-drift compensator (Olympus), a UPlansApo 100, 1.40 NA oil objective (Olympus), an Evolve 512 EMCCD camera (Roper Scientific) and an Cobolt Blues 50 mW laser (488 nm; Cobolt). Bound antibody fragments in the first frame of the time-lapse stack were tracked by a python program (https://github.com/takushim/tanitracer) as previously reported (Miyoshi et al., 2021). Dissociation rates of antibody fragments were determined by fitting the regression of bound antibody fragments to one-phase decay models:

$$y = Y0 \times e^{-k_{off} \times t}$$

using Prism 7. The dissociation rate was corrected by subtracting the photobleaching rate K from the measured k_{off} values. The half-life ($T_{1/2}$) is the time needed to let dissociate half of the probes from the targets. It is calculated as $T_{1/2} = \ln 2/k_{off}$.

Super-resolution microscopy

IRIS super-resolution was performed as previously described (Kiuchi et al., 2015). Briefly, XTC cells expressing epitope-tagged actin and focal adhesion proteins were seed on coated coverslips, fixed and blocked as above. Fixation conditions for XTC cells expressing Homer1 and VGLUT1 and primary cultured neuron were different than for the actin and focal adhesions. These cells were fixed with 4% PFA in PBS (Nacalai Tesque) containing 4% sucrose for 30 min, permeabilized with PBS containing 0.15% Triton-X100 for 10 min and blocked with 3% BSA in PBS (Zhou et al., 2019). IRIS probes were applied in 50 mM Tris buffer (pH 8.0) (Shi et al., 2010), with an oxygen scavenging mixture containing 5 U/ml pyranose oxidase (Sigma-Aldrich) (Blumhardt et al., 2018), 10 mM mercaptoethylamine (Sigma-Aldrich) (Olivier et al., 2013), 60 ug/ml catalase (Sigma-Aldrich) and 10% glucose (Olivier et al., 2013).

Single-molecule stream acquisition for primary neuron was acquired under 488-nm illumination with an Olympus IX83 inverted microscope equipped with an IX3-ZDC2 Z-drift compensator (Olympus), an UPlanApo 60x/1.50 NA oil HR objective (Olympus), ORCA-Flash4.0 V3 Digital CMOS camera (Hamamatsu). The laser system is equipped with an OBIS 488 nm 150 mW Laser (Coherent), an OBIS 552 nm 150 mW Laser (Coherent) and a gem 671 nm 750 mW Laser (Laser Quantum). For multiplexed super-resolution imaging, samples were wash 8 times with PBS before exchanging to the following probe. Bright-field images were acquired every 1 min for the correction of microscope stage drift. Spots in the single-molecule images were tracked and plotted on the blank image arrays using python programs (https://github.com/takushim/tanitracer) as previously reported (Miyoshi et al., 2021). For determination of binding events in Homer and VGLUT puncta, each binding probe was consolidated to the average position (Figures 6G, S6F, 7B, and S7). Spots which last shorter than three frames were filtered to reduce the noise and improve the localization precision. The possibility of being labelled (p) was calculated using binomial distribution:

$$p = 1 - ((m - 1)/m)^n$$

where m is the molecule number of target protein and n is the label number. One ‘‘label’’ refers to a binding (on-off) event of IRIS probe to target protein. Resolution of images were evaluated using free decorrelation analysis plugin in ImageJ (Descloux et al., 2019; Schneider et al., 2012).

QUANTIFICATION AND STATISTICAL ANALYSIS

Standard Deviations (SD) are indicated by red bars in the figures (Figures 2D, 2B, 7C, S1B, and S3B). Unpaired two-tailed t-test was used to compare the label ratio of Homer puncta between 1st antibodies (+) group and 1st antibody (–) group in Figure 7C.